RESEARCH REPORT 2015-07

APEC CLIMATE CENTER

Dynamic Downscaling of Climate Change Over The Maritime Continent

Hongwei Yang
Climate Analysis Team

APCC
APEC CLIMATE CENTER

APEC CLIMATE CENTER
RESEARCH REPORT

Dynamic Downscaling of Climate Change over the Maritime Continent

Hongwei Yang
Climate Analysis Team

RESEARCH REPORT 2015-07

APCC
APEC CLIMATE CENTER

Preface

Along with the global change, local scale climate change information is necessary to assess the impacts of changes on human life and natural environment in order to develop adaptation and mitigation strategies. Toward this aim, the COordinated Regional climate Downscaling EXperiment (CORDEX) was established. CORDEX is a World Climate Research Programme (WCRP) sponsored program to organize an international coordinated framework to produce an improved generation of regional climate change projections world-wide for input into impact and adaptation studies within the Fifth Assessment Report (AR5) of IPCC timeline and beyond. CORDEX will produce an ensemble of multiple dynamical and statistical downscaling models considering multiple forcing global climate models (GCMs) from the Coupled Model Intercomparison Project Phase 5 (CMIP5) archive. Multiple common domains covering all (or most) land areas in the world have been selected.

The Southeast Asia Regional Climate Downscaling (SEACLID) Project was developed and funded by Asia-Pacific Network (APN) for three years starting October 2013, with seven countries (i.e., Indonesia, Malaysia, the Philippines, Thailand, Vietnam, Cambodia and Lao PDR) participated. Taking advantage of SEACLID, the CORDEX Southeast Asia (CORDEX-SEA) was born to provide improved high-resolution climate project information for the local hydrological and agriculture sectors. The Asia-Pacific Economic Cooperation Climate Center (APCC) later joined the CORDEX-SEA project as one of the external institutes from outside the Southeast Asia region.

APCC has provided high-resolution climate change information for this study. This information is essential to analyze the potential climatic impacts

and adaptation measurements. Thus, the hindcast and historical downscaling experiments for the current climate were forced by reanalysis data and global model output in this study, respectively. Two climate change downscaling processes were driven by the global model projections.

We hope the results and data output from this study can provide improved climate information in high resolution for the hydrological and agriculture sectors, which may support building a long term warning system. The end-user and policy-maker might take their response options based on these reliable local scale projections.

APCC will continue to promote the best use of our research outcomes in various scientific and application areas. Our successes and achievements would not have been possible without the support of our valued partners. Beside my appreciation to APCC researchers, I extend my thanks to you and I hope you enjoy this research report.

Dr. Chin-Seung Chung
Director / APEC Climate Center
March 2015

ABSTRACT

High-resolution dynamic downscaling over the Southeast Asia domain of the COordinated Regional Climate Downscaling Experiment (CORDEX) was performed using the regional Weather Research and Forecasting (WRF) model forced by the European Centre for Medium-Range Weather Forecasts reanalysis (ERA)-Interim dataset as well as the current climate and future projections of the Hadley Centre Global Environmental Model version 2–Atmosphere–Ocean (HadGEM2–AO). Changes in the near and far future in downscaled low-level circulation and precipitation for the hindcast experiment and historical run were analyzed and compared with observations and/or corresponding large-scale forcing.

Overall compared with the hindcast experiment in 50 km resolution, not only the biases in the low-level circulation field were reduced, but also the skills of precipitation in terms of RMSE and spatial correlation coefficient were improved in the hindcast experiment with 25 km resolution in this study. The decrease of the bias is largely caused by the increase of the horizontal resolution. The WRF model reasonably reproduced the quantity and location of precipitation better than the ERA-Interim forcing. The added value over the ocean was smaller than that over land (figure not shown) owing to the biases in the lateral boundary forcing (LBF) from the ERA-Interim, lack of strong underlying forcing that may reduce errors in the WRF simulation, as well as shortage of observations over the ocean.

In the control experiment, the low-level circulation (precipitation) bias from the HadGEM2-AO was enhanced (largely reduced). The reduction occurred mainly because of the strong forcing of the underlying surface, which was better simulated in the control experiment by the increased grid resolution than in the global HadGEM2-AO.

For the future projections, the increased precipitation occurred near the climatological rain belt and the decreased precipitation occurred in the climatological dry region. The wet region became wetter and the dry region became drier in the future projection of both models. Besides the increase in the spatial variability of precipitation, the strength of both wet and dry conditions will be increased in the future under the global warming scenarios. Thus, extreme flooding or droughts will become more harmful. Generally, the two models were more consistent in projecting the mean rainfall than rainfall variability. However, both models suggested diversity among the land areas in wet and dry anomalies. In March-April-May (MAM) under scenario of RCP4.5, the Indo–China Peninsula (IC) would become slightly drier while wetter conditions would happen over Sumatra, Borneo, and New Guinea. The change over Java was uncertain. This diversity become even larger in case of the scenario RCP8.5, under which most land areas in the Maritime Continent would likely have severe drought in summer and autumn. In winter, both models suggested increase of precipitation only under the RCP4.5 scenario.

Contents

Dynamic Downscaling of Climate Change over the Maritime Continent

PREFACE i
ABSTRACT iii

1. INTRODUCTION 1

2. Model and Data 3

3. Experimental Design 6

4. Results 7
4.1 Hindcast Experiment 7
4.1.1 Low-Level Circulation 7
4.1.2 Precipitation 8
4.2 Historical Experiment 10
4.2.1 Low-Level Circulation 10
4.2.2 Precipitation 11
4.3 Future Projection 12
4.3.1 Low-Level Circulation 12
4.3.2 Precipitation 14

5. Conclusions 17

REFERENCES 20
TABLES 24
FIGURE CAPTIONS 25
FIGURES 28

1. INTRODUCTION

The Maritime Continent is a region of Southeast Asia (SEA) between the Indian and Pacific Oceans consisting of more than 10,000 islands with high topography such as Sumatra, Borneo, Java, and New Guinea. The area of shallow seas surrounding these islands is known as the Tropical Warm Pool. The global model for future climate projection predicts that the mean temperature in the Maritime Continent will increase by 2–5°C (Solomon et al. 2007), and the mean precipitation is likely to change significantly by the end of the 21st century. The Fourth Assessment Report (AR4) of the Intergovernmental Panel on Climate Change (IPCC) projections of 21st century runoff changes (Meehl et al. 2007b) showed consistency in sign among models, indicating annual mean increases in SEA. Moreover, the 2010 IPCC Special Report of Managing the Risks of Extreme Events and Disasters to Advance Climate Change Adaptation (SREX) indicated that more frequent extreme events will occur by the end of the 21st century over this region. Hence, with a population of more than half a billion and low adaptive capacity, most developing economics in the Maritime Continent are highly vulnerable to the impacts of climate change.

Due to the complexity of land–sea contrasts, with several large islands higher than 2000m, global models do not always resolve important topographic features that determine the spatial variability of rainfall at regional scales. Local error in the model over the Maritime Continent leads to systematic global uncertainties in medium-range weather prediction and climate simulation through planetary wave propagation (Peatman et al. 2013). Huge amounts of energy transferred into the atmosphere through the most prominent diurnal cycle (Kikuchi and Wang 2008; Sato et al. 2009) are accompanied by latent heat release and gravity wave disturbances. Deep cumulus convection and heavy precipitation systems influence global- and regional-scale processes such as monsoons, Madden–Julian oscillation (MJO), and El Niño Southern Oscillation (ENSO; Chang et al. 2005) and are modulated by these processes (Ichikawa and Yasunari 2008; Qian et al. 2010). Neale and Slingo (2003) observed that a heating anomaly over the Maritime Continent generates Rossby waves through divergent outflow in the model and that these waves significantly affect the thermodynamic flow over North America and the northeastern Eurasian region in winter. Qian (2008) found a dry bias accompanied by an eastward misplaced upper-

atmospheric velocity potential in a global model simulation.

The sophisticated circulation and thermodynamic forcing over the Maritime Continent create large difficulties in hydrological and agriculture management. High-resolution information is necessary for developing warning systems. Therefore, high-resolution regional climate downscaling (RCD) of climate change projection is essential for analyzing potential climatic impacts and adaptation measurements. A high-resolution model can capture local features arising from uplift condensation due to topography (Qian and Zubair 2010) to improve the predictive performance of the amplitude of the diurnal cycle and mean rainfall (Wu and Hsu 2009; Love et al 2011; Dirmeyer et al. 2012) in addition to the ratio of stratiform to convective precipitation (Boyle and Klein 2010). Fine-grid experiments reflect important topographic effects and project consistent signs of climate change (Smith et al. 2013).

Thus, the COordinated Regional Climate Downscaling Experiment (CORDEX) was established. Sponsored by the World Climate Research Programme (WCRP), CORDEX was created to organize an international coordinated framework to produce an improved generation of regional climate change projections worldwide for input into impact and adaptation studies within the Fifth Assessment Report (AR5) of the IPCC timeline and beyond. CORDEX will produce an ensemble of multiple dynamical and statistical downscaling models considering multiple forcing global climate models (GCMs) from the Coupled Model Intercomparison Project Phase 5 (CMIP5) archive. Multiple common domains covering most land areas worldwide have been selected.

In August 2012, a group of scientists from five countries including Indonesia, Malaysia, the Philippines, Thailand, and Vietnam formed the SEA Regional Climate Initiative (SEARCI), a platform for regional cooperation on climate-related research. Under this initiative, a proposal for the three-year SEA Regional Climate Downscaling (SEACLID) project was subsequently developed and funded by the Asia–Pacific Network (APN). This program began in October 2013 and added Cambodia and the Lao People's Democratic Republic (PDR). CORDEX–SEA was created to provide improved high-resolution climate project information for hydrological studies and the agriculture sector. The Asia–Pacific Economic Cooperation Climate Center (APCC) later joined the CORDEX–SEA project.

In this study, hindcast and historical downscaling experiments for the current climate are forced by reanalysis data and global model output, respectively. The two climate change downscaling processes will be driven by global model projections. The data, the evaluation method, and the experiments used in this study are described in Sections 2 and 3. The results are described in Section 4, and Section 5 presents the conclusions.

2. Model and Data

This study used the Weather Research and Forecast (WRF3.5) model (Skamarock et al. 2005), a primitive equation limited-area model under sigma coordinates. WRF is a regional prediction and downscaling system designed to meet both operational forecasting and atmospheric research needs. It has an advanced software architecture allowing parallel computing and system extendibility. Development of the state-of-the-art WRF has been undertaken as a collaborative project mainly by the National Center for Atmospheric Research (NCAR), the Forecast Systems Laboratory, the National Oceanic and Atmospheric Administration, National Centers for Environmental Prediction (NCEP), the Air Force Weather Agency (AFWA), the Naval Research Laboratory, the University of Oklahoma, and the Federal Aviation Administration. WRF allows researchers to conduct simulations reflecting real data or idealized configurations and is suitable for many applications of various scales ranging from meters to thousands of kilometers. Such applications include research and operational numerical weather prediction (NWP), data assimilation, parameterized-physics research, downscaling climate simulations, air quality models, atmosphere–ocean coupling, and idealized simulations of phenomena such as boundary-layer eddies, convection, and baroclinic waves. Two dynamics solvers are used in the WRF Software Framework (WSF): the Advanced Research WRF (ARW) solver, originally known as the Eulerian mass or “em” solver and developed primarily by NCAR, and the Nonhydrostatic Mesoscale Model (NMM) solver developed by NCEP. We selected the ARW solver for this study, in which the governing equations are compressible, nonhydrostatic Euler equations. The equations are written in flux form, and the variables satisfy conservation equations following the philosophy of Ooyama (1990). Further, the equations are expressed by using a terrain-following mass vertical coordinate (Laprise

1992). In this model, the top surface was a constant pressure surface considered to be at 50 hPa pressure. Arakawa C-grid staggering was applied for the horizontal grid. A third-order Runge–Kutta scheme with a smaller time step for acoustic and gravity-wave modes was applied for time-split integration (Klemp and Wilhelmson 1978; Skamarock and Klemp 1992; Wicker and Skamarock 2002). WRF offers multiple physical options that can be combined in any form (Skamarock et al. 2005).

In this study, we selected the WRF Single-Moment 6-Class Microphysics (WSM 6)-class graupel scheme (Hong et al. 2004) as the microphysics parameterization. This scheme includes six types of hydrometeors such as water vapor, cloud water, rain, cloud ice, snow, and graupel in six different arrays. Thus, it allows for supercooled water and gradual melting of the snow below the melting layer. In this method, mixed-phase particle fall speeds are weighted by the mixing ratios for snow and graupel particles by assigning a single fall speed to both, which is applied to both sedimentation and accretion processes. We selected the modified Tiedtke scheme (Tiedtke 1989; Zhang et al. 2011) as the cumulus parameterization. This scheme is a mass-flux type with a convective available potential energy (CAPE) removal time scale, shallow component, and momentum transport. Land surface parameterization followed the Unified Noah land-surface model (Tewari et al. 2004), which is a unified NCEP/NCAR/AFWA scheme with soil temperature and moisture in four layers, fractional snow cover, and frozen soil physics. The Yonsei University (YSU; Hong et al. 2006) planetary boundary layer (PBL) was also employed in which the counter gradient terms are used to represent fluxes owing to non-local gradients. The surface layer scheme is the fifth-generation Penn State/NCAR mesoscale model (MM5) Monin–Obukhov scheme (Paulson 1970; Dyer and Hicks 1970; Webb 1970; Beljaars 1994; Zhang and Anthes 1982) based on the Monin–Obukhov scheme with a Carslon–Boland viscous sub-layer and standard similarity functions from look-up tables. The long-wave and short-wave radiative transfer model followed the Community Atmosphere Model (CAM) scheme (Collins et al. 2004), which is based on the CAM 3 climate model used in the Community Climate System Model (CCSM). This model considers the contributions of aerosols and trace gases and uses yearly CO_2 and constant N_2O (311E-9) and CH_4 (1714E-9).

The lateral boundary forcing (LBF) fields included geopotential height, air temperature, specific humidity, and horizontal winds. The width of the buffer zone in our model was set

to 10 grid points, where the prognostic variables of the WRF model were nudged toward the large-scale forcing fields following the method of Davies and Turner (1977) with Newtonian nudging and horizontal diffusion within the regional climate model (RCM) buffer zones. The initial state conditions included the following parameters: surface pressure, sea-level pressure, 2-m-height moisture, 2-m-height temperature, 10-m-height horizontal winds, soil moisture, soil temperature, and skin temperature. The skin temperature over the ocean was considered as sea-surface temperature (SST). We obtained 30′ horizontal resolution topography and land use data in Noah land surface model (LSM) from the United States (U.S.) Geological Survey. The 30′ soil type data were obtained from the State Soil Geographic (STATSGO) database, and 5′′ global data were obtained from the Food and Agriculture Organization of the United Nations.

The European Centre for Medium-Range Weather Forecasts (ECMWF) interim reanalysis (ERA-Interim; Dee et al. 2011) dataset was used for the large-scale forcing fields for the hindcast experiment. ERA-Interim data are available from 1979 to 2013 at 6-h intervals with a horizontal resolution of 0.75° and 37 pressure levels. The output of the Hadley Centre Global Environmental Model version 2–Atmosphere–Ocean (HadGEM2-AO; Baek et al., 2012) global coupled model was used for large-scale forcing fields in the historical (control) experiment and future projection experiments. The output of HadGEM2-AO is 6-h data with a horizontal resolution of 1.25° in latitude and 1.875° in longitude. To verify the simulated circulation fields in our hindcast and historical experiments, which shows basic large-scale patterns, the seasonal mean ensemble of NCEP reanalysis 2 (NCEP-R2; Kanamitsu et al. 2002), ECMWF 40 years reanalysis (ERA-40; Uppala et al. 2011), and the Japanese 25 years reanalysis (JRA-25; Onogi et al. 2007) datasets was used as reference data. The ensemble of reanalysis datasets is more reliable than a single dataset. Due to limitations in time and computational resources, we used only the ensemble with other three reanalyses. In the future, we will introduce ERA-interim into our reference database. Seasonal mean ensemble precipitation from the Global Precipitation Climatology Project (GPCP, 2.5°× 2.5°; Adler et al. 2003), the Climate Prediction Center merged analysis of precipitation (CMAP, 2.5°× 2.5°; Xie and Arkin 1996), and the Tropical Rainfall Measuring Mission (TRMM3B43, 0.25°× 0.25°; Huffman et al. 2007) over oceans as well as the ensemble of TRMM3B43, the gauge-based analysis of Climatic Research Unit (CRU, 0.5°×

0.5°; New et al., 2002), and the Highly Resolved Observational Data Integration Towards Evaluation (APHRODITE, 0.25°× 0.25°; Yatagai et al. 2009) over land were used as the truth data for rainfall to evaluate the key variable precipitation in our hindcast and historical experiments. Compared with the ensemble of observed precipitation, the added values in the downscaling of hindcast and historical experiments were investigated by using the temporal correlation coefficient and the temporal root–mean–square error (RMSE) in March–April–May (MAM), June–July–August (JJA), September–October–November (SON), and December–January–February (DJF) seasons. Near- and far-future changes in mean and spatial variability in precipitation in the Representative Concentration Pathway (RCP) 4.5 and RCP8.5 were analyzed.

3. Experimental Design

The unique tropical climate over the Maritime Continent is very important because it is located in the most active convective area of the world and is influenced by both Hadley and Walker circulations. To consider the climate system, we required a sufficiently large domain size in which the regional model could develop its own dynamics. Therefore, our model domain covered the Maritime Continent region to extend from 15°S to 27°N and from 90°N to 145°E (Fig. 1). We selected a cylindrical equidistant map projection with a zonal and meridional grid space of approximately 0.25°. The model has 221 west–east and 169 south–north grid points and 37 sigma layers in the vertical direction up to 50 hPa.

Four experiments including the hindcast experiment, historical experiment, Down-45, and Down-85 were designed and were initiated and forced by ERA-Interim, HadGEM2-AO historical run, HadGEM2-AO RCP4.5, and HadGEM2-AO RCP8.5 future projections, respectively. In the future projection downscaling, both the LBF and the CAM3 scheme reflected concentration changes in greenhouse gases (GHGs). The prescribed SST was from the same dataset of the lateral boundary forcing for each experiment. The prefix “Down” in the experimental names refers to downscaling. The historical experiment was our control experiment, and its output was used as reference data for climate change. The physical parameterization scheme and model configuration remained the same for all experiments.

All model parameters were considered with their default values with no tuning.

The hindcast experiment was run from 1 January 1980 to 31 December 2001; the historical experiment was run from 1 January 1970 to 31 December 2005; and Down-45 and Down-85 were run from 1 January 2006 to 31 December 2100. The first year of the hindcast and historical experiments was considered as a "spin-up" period; the model outputs from the second year were analyzed. The near and far futures were defined as periods of 2021–2050 and 2071–2100, respectively. The historical reference data for studying climate change were taken for the period 1971–2000, a sub-period of the historical experiment.

4. Results

4.1 Hindcast Experiment

4.1.1 Low-Level Circulation

To evaluate the circulation fields simulated in the hindcast experiment, we used the ensemble mean of NCEP-R2, ERA-40, and JRA-25 datasets as the reference dataset.

In MAM (Fig. 2a), except for a weak positive geopotential height occurring over the Indo–China Peninsula (IC) at 850 hPa, the WRF model produced reasonable results over most areas with biases of less than 5 m in terms of geopotential height. In JJA (Fig. 2b), a weak negative geopotential height bias at 850 hPa was noted with a cyclone anomaly over the IC and the South China Sea (SCS). In SON and DJF (Figs. 2c and 2d), similar positive biases in geopotential height occurred over the northern part of the IC, whereas no organized biases were noted over the SCS. The entire field of geopotential height generally showed a positive anomaly in the east and a negative anomaly in the west, which may have been caused by systematically internal dynamic biases in the WRF model. Errors of the same type were reported by Yang (2013). Overall, the downscaling bias in the hindcast experiment with 25-km resolution in this study was much smaller than that of Yang (2013) with 50-km resolution. The decrease in bias was caused largely by the increase in horizontal resolution, although the slightly different model domains adopted in these two studies were forced with similar reanalyses from ECMWF. Here, our objective

is to show improvement in the progress of CORDEX–SEA, which may be achieved from different experiments; further effort is needed to fully address these biases. The improved downscaling performance provided significantly more confidence to study climate change in the future projection.

4.1.2 Precipitation

To verify the simulated precipitation in the hindcast experiment, the observed climatological seasonal mean of rainfall was used as the reference dataset. This dataset was derived from the ensemble mean of CRU, APHRODITE, and TRMM over land and CMAP, GPCP, and TRMM over the ocean.

To investigate the added value in the hindcast experiment, we adopted two criteria calculated through multi-year seasonal data from the output of the WRF model and its forcing, the ERA-Interim. For example, let $\boldsymbol{r}_{wrf}$ and $\boldsymbol{r}_{era}$ be the temporal correlation coefficients of the output of WRF and ERA-Interim, respectively, relative to the verification of precipitation. Let $r_t = \boldsymbol{r}_{wrf} - \boldsymbol{r}_{era}$; then, the positive value of $\boldsymbol{r}_t$ is the added value. Similarly, let $\boldsymbol{e}_{wrf}$ and $\boldsymbol{e}_{era}$ be the RMSE in the temporal dimension of the output from the WRF and ERA-Interim relative to the verification precipitation. Because $\boldsymbol{e}_t = \boldsymbol{e}_{era} - \boldsymbol{e}_{wrf}$, the positive value of $\boldsymbol{e}_t$ represents the added value; this indicates that RSME in the WRF model was smaller than that in the ERA-Interim. Both r_t and $\boldsymbol{e}_t$ maps showed positive values indicating the added values (Figs. 3 and 4). Moreover, $\boldsymbol{e}_t$ is equal to the difference of spatial RMSE.

The r_t shown in Fig. 3 indicates that the hindcast experiment yielded added values in MAM over a large part of Sumatra and New Guinea as well as over part of the IC. In JJA, the WRF model yielded added value of r_t over part of the IC and Borneo as well as large part of Sumatra, New Guinea. The amplitude of the added value in JJA was similar to that in MAM. In SON, the added values were shown over parts of the IC and large parts of Sumatra, Borneo, and New Guinea. In DJF, added values were observed over a large part of the IC and parts of Sumatra, Borneo, Java, and New Guinea.

In terms of $\boldsymbol{e}_t$ (Fig. 4), the hindcast experiment results in MAM showed added values over almost all land areas. The added values were high over Sumatra, Java, Borneo, and

New Guinea. In JJA, added values were found over most land areas with very high values noted over the IC, northern Borneo, and central New Guinea. In SON, the WRF model yielded added values over most land areas with large values over the southern IC, most parts of Sumatra, Borneo, and Java, and parts of New Guinea. In DJF, except for the IC where small added values were found, large added values were noted over most of Sumatra, Java, Borneo, and New Guinea. The seasonal variability of the added values moved with the precipitation band, which was caused by the better-designed cumulus physical package and the realistic setup of the underlying forcing in the RCM. The locations and times of rainfall were captured more realistically in the RCM than that by large-scale forcing.

The added values of e_t indicate that the WRF model reasonably reproduced the quantity and location of precipitation better than the ERA-Interim. The added value over the ocean was smaller than that over land (figure not shown) because the prescribed SST cannot be adjusted to the behavior of the atmosphere only model. In addition, the lack of strong underlying forcing may have been disadvantageous to the WRF model, and fewer observations were available over the ocean.

The downscaling performance forced by the reanalysis datasets under 50-km and 25-km horizontal resolutions was also compared. Table 1 shows the spatial correlation coefficients (Rs) of both hindcast experiments under the different resolutions. Rs in all cases in the experiment at 25-km resolution was larger than that at 50-km resolution. Table 2 compares the spatial RMSE (Es) of the two hindcast experiments. In MAM, the finer-resolution experiment did not show improved performance over that with lower resolution. In JJA, the 25-km-grid experiment outperformed that at 50-km over both land and oceans and thus over the entire domain. In SON, the experiment with the 25-km grid was better than the than that at 50 km over oceans and the entire domain except for land. In DJF, the finer resolution improved only over land. Overall, the finer-resolution experiment was not better than that with low resolution in terms of Es. However, in all cases in which the finer-resolution experiment was better, the low-resolution experiment had significantly large errors. That is, the large errors were reduced with an increase in downscaling resolution.

The low-level circulation bias in the hindcast experiment was reasonably small except over the northern IC. The precipitation bias in the HadGEM2-AO was reduced in the WRF

model largely because of the strong forcing of the underlying surface; this forcing was better simulated in the hindcast experiment than in the ERA-Interim reanalysis. Compared with the low-resolution hindcast experiment, the spatial correlation coefficients were improved overall. In terms of RMSE, all of the large errors were reduced in the finer-resolution hindcast experiment.

4.2 Historical Experiment

4.2.1 Low-Level Circulation

Unlike the ensemble mean of the three reanalysis datasets, the HadGEM2-AO produced a negative geopotential height bias at 850 mb over a large part of the domain with a westerly anomaly over the Indian Ocean in the Southern Hemisphere and an easterly anomaly over the equatorial Pacific in MAM (Fig. 5a). An additional cyclonic anomaly was observed over the IC and the northern SCS. The historical downscaling experiment of the WRF model (control experiment) showed an enhanced negative geopotential height anomaly over the western domain in MAM. The easterly anomaly over the equatorial Pacific was also intensified (Fig. 5b).

In JJA, HadGEM2-AO produced a strong easterly anomaly accompanied by a negative geopotential height anomaly over the northern domain (Fig. 5c), which was enhanced in the control experiment. Geopotential height anomalies deeper than 10 m were observed over most of the domain (Fig. 5d). In SON, HadGEM2-AO produced a positive geopotential height anomaly over the southwestern domain and a strong negative anomaly over the northeastern domain (Fig. 5e). In the control experiment, the negative anomaly in HadGEM2-AO was concentrated and enhanced to the west over the SCS. The positive anomaly in HadGEM2-AO was also enhanced in the control experiment (Fig. 5f). In DJF, HadGEM2-AO produced a negative geopotential height anomaly around 110° E throughout the domain (Fig. 5g), which was enhanced in the control experiment. The easterly anomaly in HadGEM2-AO over the equatorial Pacific shifted to the east in the control experiment (Fig. 5h).

Upon forcing by the output of HadGEM2-AO, which effectively simulates surface temperature (Baek et al 2013), the biases in low-level circulation in the control experiment were larger than those originally existing in HadGEM2-AO. This occurred because the

WRF model was unable to reduce the uncertainties in the LBF; therefore, the biases in the control experiment were larger than those in the hindcast experiment forced by the reanalysis dataset. Under similar lower boundary forcing, the biases in the LBF from HadGEM2-AO were the main cause of the deteriorated performance of the WRF model in the control experiment.

4.2.2 Precipitation

The verification data of precipitation in the control experiment were the same as those used in the hindcast experiment. The only difference between the two data sets was that the period considered in the historical experiment was from 1971 to 2000.

The positive r_t shown in Fig. 6 indicates that the control experiment yielded added values in MAM over a large part of the IC and New Guinea and part of Java. In JJA, the WRF model yielded added value of r_t over parts of the IC, Sumatra, Borneo, and New Guinea and all of Java. In SON, the added values were shown over part of the IC, large parts of Borneo and Sumatra, and all of Java. In DJF, added values were observed over the southeastern part of the IC, large parts of Sumatra and Borneo, and the middle part of New Guinea.

In terms of e_t (Fig. 7), the control experiment results showed added values in MAM over large parts of the IC, Sumatra, Borneo, and Java and the central part of New Guinea. In JJA, very high values were observed over parts of the eastern IC and central New Guinea; added values were also observed over large parts of Sumatra and Borneo. In SON, the WRF model yielded added values over the southern IC, nearly all of Borneo and Java, and parts of Sumatra and New Guinea. In DJF, the WRF model produced added values only over Java, most of Borneo, and parts of Sumatra and New Guinea. Over the IC, only a small region had small added values of e_t. The added values also shifted with seasonal movement of the precipitation band, which means that the WRF model simulated the mechanism of precipitation better than HadGEM2-AO.

The added value over the ocean was poor (figure not shown) because the SST cannot be adjusted to the WRF model in this atmosphere-only system. In addition, the lack of strong topography forcing may have been disadvantageous to the WRF model. The low-level circulation bias from HadGEM2-AO was enlarged in the control experiment, whereas the

precipitation bias in the former was reduced in the latter. This reduction occurred largely because of the strong forcing of the underlying surface; the forcing was better simulated in the control experiment than in the global HadGEM2-AO.

4.3 Future Projection

4.3.1 Low-Level Circulation

We analyzed the low-level circulation changes in RCP4.5 and RCP8.5 projection for the periods 2021–2050 (near future) and 2071–2100 (far future) for the HadGEM2-AO and WRF simulations relative to their historical periods.

In the RCP4.5-projected near future in MAM (Fig. 8a), the change in geopotential height at 850 hPa in HadGEM2-AO was significantly positive over the entire domain. The largest change occurred over the northern SCS and the northern Philippine Sea, where a significant easterly wind change took place. The downscaled result was consistent with that of HadGEM2-AO, with smaller but significant increases in geopotential height over the entire domain. Conversely, a significant westerly wind anomaly occurred over the tropical Pacific (Fig. 8b), which indicates a future weakening in the tropical easterly wind (e.g. Vecchi and Soden 2007). In the RCP8.5-projected near future in MAM (Fig. 8c), HadGEM2-AO produced a slightly larger increase in height than that in the case of RCP4.5 with a significant easterly wind increase over the Indian Ocean. The WRF model enhanced the changes in the case of RCP4.5 (Fig. 8d).

In the RCP4.5-projected far future in MAM (Fig. 8e), the geopotential height increased by more than 12 m over most parts of the domain with significant wind changes over several areas. The WRF model consistently increased the height with the maximum change over the northeastern domain. Significant wind changes occurred over the Indian Ocean and tropical Pacific (Fig. 8f). In the RCP8.5-projected far future in MAM (Figs. 8g and 8h), the HadGEM2-AO and WRF models enhanced the changes in RCP4.5 cases. A significantly strong anticyclonic anomaly over the IC is shown to dramatically decrease the local precipitation (Fig. 8h).

In the RCP4.5-projected near future in JJA (Fig. 9a), HadGEM2-AO produced a weak but significantly positive change in geopotential height at 850-hPa over most of the

domain. Significant northeastern wind anomalies occurred over the Bay of Bengal (BOB), the Philippines, and the adjacent ocean. The WRF model reproduced the significantly positive change in geopotential height over most of the domain except for the northeastern boundary. A significant westerly wind change occurred over the tropical Pacific (Fig. 9b). In the RCP8.5-projected near future in JJA (Figs. 9c and 9d), the HadGEM2-AO and WRF models produced consistently significant easterly wind changes over the BOB and SCS. The positive changes of geopotential height in both models increased consistently compared with the respective results of RCP4.5.

In far-future changes (Figs. 9e–h) for each model and each scenario, significant changes were mostly consistent but were enhanced over the corresponding changes in the near future. However, the significant changes around the IC were enclosed in an anticyclonic circulation, which will produce significant drying of the IC, northern Sumatra, and Borneo in the far future in JJA.

In the RCP4.5-projected near future in SON (Fig. 10a), HadGEM2-AO produced a significant uniform positive change in geopotential height at 850-hPa over the entire domain with significant northwestern wind changes around 5m/s. The WRF model produced changes consistent with the HadGEM2-AO (Fig. 10b), particularly for the wind field over the ocean between Borneo and New Guinea. In the RCP8.5 projected near future in SON (Fig. 10c), HadGEM2-AO produced a positive change in height with an anticyclone centered over the IC and the SCS. The WRF model produced a positive height change centered over the Indian Ocean in the Southern Hemisphere (Fig. 10d).

In the RCP4.5-projected far future in SON (Fig. 10e), HadGEM2-AO produced a positive height change over the entire domain with significant wind changes around the equatorial ocean. The WRF model produced significantly strong westerly changes over the IC and the adjacent ocean and featured enhanced changes over the near-future case (Fig. 10f). In the RCP8.5-projected far future in SON (Fig. 10g), both HadGEM2-AO and WRF models enhanced the significant change patterns noted in the RCP4.5 scenarios. The difference between the two models was pronounced over the IC and the equatorial Indian Ocean. The WRF model shifted the significant northwesterly wind change to its north over the northern West Pacific (Fig. 10h).

In the RCP4.5-projected near future in DJF (Fig. 11a), the HadGEM2-AO and WRF models produced uniform positive changes in height. The significant wind change in HadGEM2-AO blew from the east over the northern West Pacific, whereas the significant wind change blew from the west over the Equatorial Pacific in the WRF model. In the RCP8.5-projected near future in DJF (Figs. 11c, 11d), both models enhanced the significant height changes. HadGEM2-AO produced a significant westerly change over the equatorial region (Fig. 11c), which is more strongly consistent to the change in the WRF model (Fig. 11d) than that in the case of RCP4.5.

In the RCP4.5- and RCP8.5-projected far future in DJF (Figs. 11e and 11g), HadGEM2-AO enhanced the change patterns in the near future. The WRF model produced significant wind change over more areas than that in the near-future case. The downscaled change patterns in RCP4.5 and RCP8.5 of the WRF model were similar but showed different change levels.

4.3.2 Precipitation

We analyzed changes in precipitation in terms of the climatological seasonal mean and spatial variability in RCP4.5 and RCP8.5 projections for 2021–2050 (near future) and 2071–2100 (far future) for both HadGEM2-AO and WRF simulations relative to their historical experiments.

Precipitation in the future projection of HadGEM2-AO in MAM generally decreased significantly over southern China and near Taiwan, although it significantly increased over the equatorial region and the southern Indian Ocean. Both models were largely consistent in projecting the wet and dry regions. The WRF model consistently projected drier condition over the southern IC, which is consistent with the downscaled circulation field. The significantly increased precipitation over the Philippine Sea (Fig. 12b) only occurred in the far future or high-level density of GHGs in HadGEM2-AO (Figs. 12c, 12g), although it occurred in the near future under a less-dense level of GHGs (RCP4.5) in the WRF model (Fig. 12b). Therefore, the WRF model is more sensitive than HadGEM2-AO to GHGs. Under RCP4.5 in the near future, both models projected the significantly increased precipitation over the equatorial region and the significantly decreased precipitation near

the southern boundary. Under RCP8.5 in the far future, both models generally projected the same significant precipitation change. However, the WRF model projected significantly dry conditions over the SCS and the Taiwan Strait.

In JJA, both models generally agreed on the northward shift of the wetter region along with the shift of the Intertropical Convergence Zone (ITCZ) in the boreal summer relative to spring. The projected drier region was generally situated south of the equator; however, the WRF model indicated an additional drier zone from west to east along the IC, SCS, and Philippine Sea in the far future. Both models showed a strong drought anomaly over the southern IC in the far future under RCP8.5. Because of the northward shift of the change, most land would experience drier conditions in JJA.

In SON, the significant dry anomaly occurred over the southern Indian Ocean in both models in the far future and in the near future for RCP8.5. No significant drier conditions over the IC were noted in SON. Instead, both models projected significantly wetter conditions over the IC in the far future. HadGEM2-AO produced a wet anomaly north of the equator. Except for the IC, most of the land would experience drier conditions in this season.

In DJF, the precipitation projected by the HadGEM2-AO and WRF models decreased significantly over the ocean near the northern boundary and was mostly similar over southern Borneo, Sumatra, Java, and the southern Indian Ocean. The precipitation significantly increased mostly over the IC, SCS, and the Philippine Sea. Different from MAM, JJA, and SON, the region of precipitation increase was not well overlapped with the rain band, which indicates that the change was delayed relative to the rain band southern movement in DJF.

Essentially, the increased precipitation occurred around the climatological rain belt and the decrease of precipitation occurred in the climatological dry region. The wet (dry) region became wetter (drier) in the future projection of both models. Besides the effects of increasing the spatial variability of precipitation, the above conclusions also indicate that the strength of both wet and dry conditions would be stronger in the future under the global warming assumption. Thus, extreme flooding or droughts would become more dangerous.

Land-only precipitation change is shown in Fig. 16, and Fig. 17 shows changes in spatial variability of the land rainfall. In case of near future under RCP4.5, the HadGEM2-AO and WRF models consistently projected the increase in precipitation over Sumatra, Borneo, and New Guinea in MAM and consistently projected the decrease in precipitation over the IC. The HadGEM2-AO and WRF models projected the increase in precipitation variability over most land areas except for the IC (Fig. 17). In JJA, diversity in the sign of projected changes between HadGEM2-AO and WRF was quite large. The models projected a consistent decrease in precipitation only over the IC and Java. In SON, both models consistently projected the increase signal of precipitation over all land areas, particularly over Sumatra and Borneo. In JJA and SON, the variability changes in precipitation in HadGEM2-AO were very small. WRF projected a decrease in precipitation variability over New Guinea in summer and an increase in precipitation variability over Sumatra and Borneo in autumn (Fig. 17). In DJF, both models consistently projected an increase in precipitation over most land areas except for New Guinea. HadGEM2-AO projected a slight increase in precipitation variability over all land areas, whereas the WRF model projected a decrease in precipitation variability over Sumatra (Fig. 17).

In case of far future under RCP4.5, the quantity of change was obviously larger than that in the near-future case; however, the consistency between the two models was not decreased. In MAM, both models strongly agreed in projecting the increase in precipitation over Sumatra, Borneo and New Guinea and for the decrease in precipitation over the IC and Java. Except for IC, both models projected increases in precipitation in JJA over Sumatra and Borneo and decreases over Java. Over New Guinea, the precipitation decrease in the WRF simulation was significantly greater than that in the HadGEM2-AO simulation. In SON, both models projected very small changes in of precipitation, which indicates strong agreement. In DJF, both models consistently projected increases in precipitation over all land areas. In all seasons, HadGEM2-AO projected very small changes in rainfall variability, whereas WRF tended to increase the rainfall variability over most land areas (Fig. 17).

In the case of near future under RCP8.5, both models consistently projected a decrease in rainfall over the IC and Java; the WRF model showed a significant decrease in rainfall over Java in MAM compared with the HadGEM2-AO results. In JJA, both models

consistently projected decreases in rainfall over most land areas except for Borneo, where the change sign of the two models was different but both quantities were small. In SON, both models simulated decreases in rainfall over most land areas. In DJF, the quantity of precipitation change was very small in the projections of both models over all land areas. HadGEM2-AO projected a slight increase in rainfall variability in most seasons, whereas WRF decreased the rainfall variability most of the time (Fig. 17).

In case of far future under RCP8.5, both models projected large decreases in precipitation over Java in MAM. In JJA and SON, both models projected large dry anomalies in most cases, which indicates that most land areas over the Maritime Continent would likely incur severe, lengthy droughts in SON until DJF in the far future under RCP8.5. HadGEM2-AO projected small changes in rainfall variability most of the time except over Java in DJF; WRF projected large changes in rainfall variability in many cases (Fig. 17).

Generally, the two models were more consistent in the projection of mean rainfall than that of rainfall variability. Under the RCP4.5 scenario, the wet and dry anomalies over the land areas differed significantly for both models in MAM. The IC would become slightly drier, whereas wetter conditions would occur over Sumatra, Borneo, and New Guinea. The change over Java was uncertain. This diversity became even larger under the scenario of RCP8.5, where most land areas in the Maritime Continent would likely have severe drought in JJA and SON. In DJF, both models showed an increase in precipitation only under the RCP4.5 scenario.

5. Conclusions

To study the impact of climate change over the Maritime Continent, four regional climate dynamic downscaling experiments were conducted with the WRF model. The hindcast and historical downscaling experiments for current climate were forced by reanalysis data and the global model output of HadGEM2-AO, respectively. Two climate change downscaling experiments were driven by the global model projections from HadGEM2-AO. This study provides the preliminary results and an insight into the dynamic downscaling approach for flooding and drought applications.

Compared with the hindcast experiment reported by Yang (2013), errors in the low-level wind field and geopotential height were generally reduced, and the skills of precipitation in terms of spatial RMSE and correlation coefficient were improved in the hindcast experiment under 25-km resolution in the present study. This decrease in error is attributed mainly to the increase in horizontal resolution. The added values on RMSE indicated that the WRF model reasonably reproduced the quantity and timing of precipitation better than the ERA-Interim forcing. The added value over the ocean was less (figure not shown), owing to biases in the large-scale forcing field derived from the ERA-Interim data. In addition, the lack of strong topographic forcing and the shortage of ground truth observations over the ocean may lead the increased errors in WRF simulation. The biases in low-level circulation field of large-scale forcing by HadGEM2-AO were enlarged by the WRF model in the historical experiment, whereas the precipitation biases in this large-scale forcing were significantly reduced. This reduction was caused mainly by the strong topographic forcing from the underlying surface, which was better recognized in RCD by increasing the gird resolution. The added values in the hindcast and historical experiments provided confidence for further study in climate change projection through the RCD approach.

Essentially, the precipitation increased around the climatological rain belt and decreased over the dry climate region in the future projections. The wet (dry) region became wetter (drier) in the future projections of both models, which is consistent with the large-scale projection of the GCM. The temperature will increase, and dry areas with higher evaporation than precipitation will evaporate to provide more moisture to the air and will thus become drier. The wet areas in which the convection contains more moisture, as shown by absolute humidity increases from RCP4.5 to RCP8.5, will produce more precipitation. Beside the effects of increasing the spatial variability of precipitation, the above conclusion also indicates that the strength of both wet and dry conditions would be increased in the future. Thus, extreme flooding or droughts would become more dangerous. Generally, the mean rainfall was more consistently projected than rainfall variability in the two models. In DJF, both models suggested an increase in precipitation only under the RCP4.5. The wet and dry anomalies simulated over land differed significantly in both models in MAM under RCP4.5. The IC would become slightly drier, whereas wetter

conditions would occur over Sumatra, Borneo, and New Guinea. This diversity become even larger in the case of RCP8.5, in which most land over the Maritime Continent would likely incur severe droughts in JJA and SON.

Because the land distribution is highly complicated over the Maritime Continent with many small islands, the 25-km resolution in our experiments is still insufficient due to limitations in available computational resources. Because air–sea interaction was not considered, the bias in the prescribed SST from the large-scale model persisted throughout the entire period of our downscaling experiments and influenced the thermodynamic balance of the circulation. A coupled regional climate model may solve this problem. Moreover, the bias originating from LBF also requires reduction in future experiments.

REFERENCES

Adler R. F., G. J. Huffman, D. T. Bolvin et al., 2000: Tropical rainfall distributions determined using TRMM combined with other satellite and rain gauge information. *J. Appl. Meteor.*, **39**, 2007–2023.

Adler R. F., G. J. Huffman, A. Chang, et al., 2003: The version-2 global precipitation climatology project (GPCP) monthly precipitation analysis (1979–present). *J. Hydrometeor.*, **4**, 1147–1167.

Baek, H. J., and Coauthors, 2013: Climate change in the 21st century simulated by HadGEM2-AO under representative concentration pathways. *Asia Pac J. Atmos. Sci.*, 1–16.

Beljaars, A. C. M., 1994: The parameterization of surface fluxes in large-scale models under free convection. *Quart. J. Roy. Meteor. Soc.*, **121**, 255–270.

Boyle, J., and S. A. Klein, 2010: Impact of horizontal resolution on climate model forecasts of tropical precipitation and diabatic heating for the TWP. *Journal of Geophysical Research: Atmospheres*, **115**(D23)

Chang, C. P., P. A. Harr, and H. J. Chen, 2005: Synoptic disturbances over the equatorial South China Sea and western Maritime Continent during boreal winter. *Mon. Wea. Rev.*, **133**(3), 489–503.

Collins, William D., et al., 2004: Description of the NCAR Community Atmosphere Model (CAM 3.0). NCAR Tech. Note NCAR/TN–464+STR, 214 pp.

Dee, D. P., and Coauthors, 2011: The ERA-Interim reanalysis: configuration and performance of the data assimilation system. *Quart. J. Roy. Meteor. Soc.*, **137**, 553–597.

Dirmeyer, P. A., and Coauthors, 2012: Simulating the diurnal cycle of rainfall in global climate models: resolution versus parameterization. *Climate Dynam.*, **39**(1–2), 399–418.

Dyer, A. J., and B. B. Hicks, 1970: Flux–gradient relationships in the constant flux layer. *Quart. J. Roy. Meteor. Soc.*, **96**, 715–721.

Fu, X., B. Wang, and T. Li, 2002: Impacts of Air-Sea Coupling on the Simulation of Mean Asian Summer Monsoon in the ECHAM4 Model*. *Mon. Wea. Rev.*, **130**(12), 2889–2904.

Fu, X., and B. Wang, 2004: Differences of Boreal Summer Intraseasonal Oscillations Simulated in an Atmosphere–Ocean Coupled Model and an Atmosphere-Only Model. *J. Climate*, **17**, 1263–1271.

Hong, S.-Y., J. Dudhia, and S.-H. Chen, 2004: A Revised Approach to Ice Microphysical Processes for the Bulk Parameterization of Clouds and Precipitation. *Mon. Wea. Rev.*, **132**, 103–120.

Hong, S.-Y., Y. Noh, and J. Dudhia, 2006: A new vertical diffusion package with an explicit treatment of entrainment processes. *Mon. Wea. Rev.*, **134**, 2318–2341.

Huffman, G. J., and Coauthors, 2007: The TRMM Multisatellite Precipitation Analysis (TMPA): Quasi-global, multiyear, combined-sensor precipitation estimates at fine scales. *J. Hydrometeor.*, **8**, 38–55.

Ichikawa, H., and T. Yasunari, 2008: Intraseasonal Variability in Diurnal Rainfall over New Guinea and the Surrounding Oceans during Austral Summer. *J. Climate*, **21**, 2852–2868.

Kikuchi, K., and B. Wang, 2008: Diurnal precipitation regimes in the global tropics*. *J. Climate*, **21**(11), 2680–2696.

Love, B. S., A. J. Matthews, and G. Lister, 2011: The diurnal cycle of precipitation over the maritime continent in a high-resolution atmospheric model. *Quart. J. Roy. Meteorol. Soc.*, **137**, 934-947.

New, M., D. Lister, M. Hulme, and I. Makin, 2002: A high-resolution data set of surface climate over global land areas. *Climate Res.*, **21**(1), 1–25.

Neale, R., and J. Slingo, 2003: The maritime continent and its role in the global climate: A GCM study. *J. Climate*, **16**(5), 834–848.

Meehl, G. A., et al., 2007b: Global climate projections. In: Climate Change 2007: The Physical Science Basis. Contribution of Working Group I to the Fourth Assessment Report of the Intergovernmental Panel on Climate Change [Solomon, S., D. Qin, M. Manning, Z. Chen, M. Marquis, K. B. Averyt, M. Tignor and H. L. Miller (eds.)] Cambridge University Press, Cambridge, United Kingdom and New York, NY, USA, pp. 747–846.

Mori, S., and Coauthors, 2004: Diurnal land–sea rainfall peak migration over Sumatera Island, Indonesian maritime continent, observed by TRMM satellite and intensive rawinsonde soundings. *Mon. Wea. Rev.*, **132**(8), 2021–2039.

Paulson, C. A., 1970: The mathematical representation of wind speed and temperature profiles in the unstable atmospheric surface layer. *J. Appl. Meteor.*, **9**, 857–861.

Peatman, S. C., A. J. Matthews, and D. P. Stevens, 2013: Propagation of the Madden–Julian Oscillation through the Maritime Continent and scale interaction with the diurnal cycle of precipitation. *Quart. J. Roy. Meteor. Soc.*, **140**(680), 814-825.

Qian, J. H., 2008: Why precipitation is mostly concentrated over islands in the Maritime Continent. *J. Atmos. Sci.*, **65**(4), 1428–1441.

Qian, J. H., and L. Zubair, 2010. The effect of grid spacing and domain size on the quality of ensemble regional climate downscaling over South Asia during the northeasterly monsoon. *Mon. Wea. Rev.*, **138**(7), 2780–2802.

Qian, J. H., A. W. Robertson, and V. Moron, 2010: Interactions among ENSO, the monsoon, and diurnal cycle in rainfall variability over Java, Indonesia. *J. Atmos. Sci.*, **67**(11), 3509–3524.

Sato, T., H. Miura, M. Satoh, Y. N. Takayabu, and Y. Wang, 2009: Diurnal cycle of precipitation in the tropics simulated in a global cloud-resolving model. *J. Climate*, **22**(18), 4809–4826.

Smith, I., Moise, A., Katzfey, J., Nguyen, K., & Colman, R. 2013: Regional-scale rainfall projections: Simulations for the New Guinea region using the CCAM model. Journal of Geophysical Research: Atmospheres, **118**(3), 1271-1280.

Solomon, S., D. Qin, M. Manning, Z. Chen, M. Marquis, K. B. Averyt, M. Tignor, and H. L. Miller. (2007). Climate change 2007—the physical science basis: Working group I contribution to the fourth assessment report of the IPCC (Vol. 4). Cambridge University Press, Cambridge, United Kingdom, and New York, NY, USA.

Tewari, M., and Coauthors, 2004: Implementation and verification of the unified NOAH land surface model in the WRF model. 20th Conference on Weather Analysis and Forecasting/16th Conference on Numerical Weather Prediction, pp. 11–15.

Tiedtke, M., 1989: A comprehensive mass flux scheme for cumulus parameterization in large–scale models. *Mon. Wea. Rev.*, **117**, 1779–1800.

Uppala, S. M., and Coauthors, 2005: The ERA-40 re-analysis. *Quart. J. Roy. Meteor. Soc.*, **131**, 2961–3012.

Webb, E. K., 1970: Profile relationships: The log-linear range, and extension to strong stability. *Quart. J. Roy. Meteor. Soc.*, **96**, 67–90.

Vecchi, G. A., and B. J. Soden, 2007: Global warming and the weakening of the tropical circulation. *J. Climate*, 4316–4340.

Wu, C. H., and H. H. Hsu, 2009: Topographic influence on the MJO in the Maritime Continent. *J. Climate*, **22**(20), 5433–5448.

Xie P., and P. A. Arkin, 1996: Global precipitation: A 17-year monthly analysis based on gauge observations, satellite estimates, and numerical model outputs. *Bull. Amer. Meteor. Soc.*, **78**, 2539–2558.

Yang, H.-W., 2013: Revision of Climate Change by Dynamic Downscaling over the Maritime Continents. APCC Tech. Report

Yatagai, A., O. Arakawa, K. Kamiguchi, H. Kawamoto, M. I. Nodzu, and A. Hamada, 2009: A 44-year daily gridded precipitation dataset for Asia based on a dense network of rain gauges. *SOLA*, **5**, 137–140.

Zhang, Chunxi, Yuqing Wang, and Kevin Hamilton, 2011: Improved representation of boundary layer clouds over the southeast pacific in ARW–WRF using a modified Tiedtke cumulus parameterization scheme. Mon. Wea. Rev., **139**, 3489–3513.

Zhang, D.–L., and R.A. Anthes, 1982: A high–resolution model of the planetary boundary layer– sensitivity tests and comparisons with SESAME–79 data. *J. Appl. Meteor.*, **21**, 1594–1609.

Zhou, L., and Y. Wang, 2006: Tropical Rainfall Measuring Mission observation and regional model study of precipitation diurnal cycle in the New Guinean region. *J. Geophys. Res. Atmos.* (1984–2012), **111**(D17).

TABLES

Table 1. Spatial correlation coefficients (*Rs*) of seasonal precipitation in the hindcast downscaling experiments under horizontal resolutions of 50 km and 25 km relative to observations in March–April–May (MAM), June–July–August (JJA), September–October–November (SON), and December–January–February (DJF) over the entire domain, land regions, and ocean area.

Rs (0.5/0.25)	All	Land	Ocean
MAM	0.68/0.80	0.54/0.72	0.72/0.84
JJA	0.75/0.76	0.62/0.64	0.80/0.81
SON	0.75/0.83	0.61/0.71	0.78/0.87
DJF	0.79/0.85	0.68/0.81	0.83/0.87

Table 2. Spatial root–mean–square error (RMSE; *Es*, in unit of mm d^{-1}) of seasonal precipitation of the hindcast downscaling experiments in 50-km and 25-km horizontal resolutions relative to the observations in March–April–May (MAM), June–July–August (JJA), September–October–November (SON), and December–January–February (DJF) over the entire domain, land regions, and ocean area.

Es (0.5/0.25)	All	Land	Ocean
MAM	2.65/3.27	3.31/3.65	2.48/3.14
JJA	6.20/4.31	4.75/4.18	6.46/4.35
SON	4.07/3.58	3.34/3.83	4.21/3.50
DJF	3.25/3.41	4.10/3.82	3.03/3.27

FIGURE CAPTIONS

Figure 1 Simulation domain (15°S–27°N, 90–145°E), buffer zone (outside of blue dashed lines: 12.5°S–24.5°N, 87.5–142.5°E), and topography (color shading in units of m). Analysis areas over land enclosed by blue lines refer to the Indo–China Peninsula (IC), Sumatra, Java, Borneo, and New Guinea.

Figure 2 Model biases of geopotential height (shading in units of m) and horizontal winds (vector in units of 5 m s^{-1}) at 850 hPa in (a) March–April–May (MAM) mean, (b) June–July–August (JJA) mean, (c) September–October–November (SON) mean, and (d) December–January–February (DJF) mean in the hindcast experiment forced by the European Centre for Medium-Range Weather Forecasts (ECMWF) Interim reanalysis (ERA-Interim). All of the biases are defined by the departure of regional climate model (RCM) simulations from the large-scale forcing of ensemble mean of the National Centers for Environmental Prediction/Department of Energy (NCEP/DOE) reanalysis 2 (NCEP-R2), ERA 40 years (ERA-40), and Japanese 25-year reanalysis (JRA-25). White zones indicate the missing values masked by the topography.

Figure 3 Differences between temporal correlation coefficients of the seasonal precipitation in the hindcast experiment and the European Centre for Medium-Range Weather Forecasts (ECMWF) Interim reanalysis (ERA-Interim) over land in March–April–May (MAM), June–July–August (JJA), September–October–November (SON), and December–January–February (DJF) relative to the verification of precipitation. Positive values indicate that the correlation coefficients of the hindcast experiments are larger than those of the ERA-Interim.

Figure 4 Differences between the temporal root–mean–square error (RMSE) of the seasonal precipitation in the hindcast experiment and the European Centre for Medium-Range Weather Forecasts (ECMWF) Interim reanalysis (ERA-Interim) over land in March–April–May (MAM), June–July–August (JJA), September–October–November (SON), and December–January–February (DJF) relative to the verification of precipitation. Positive values indicate that the RMSE of the hindcast experiment are less than those of the ERA-Interim.

Figure 5 Model biases of geopotential height (shading in units of m) and horizontal winds (vector in units of 5 m s^{-1}) at 850 hPa of the Hadley Centre Global Environmental Model version 2–Atmosphere–Ocean (HadGEM2-AO) and historical experiment in (a), (b) March–April–May (MAM) mean; (c), (d) June–July–August (JJA) mean; (e), (f) September–October–November (SON) mean; and (g), (h) December–January–February (DJF) mean. All of the biases are defined by the departure from large-scale forcing of the ensemble mean of National Centers for Environmental Prediction/Department of Energy (NCEP/DOE) reanalysis 2 (NCEP-R2), European Centre for Medium-Range Weather Forecasts 40-year reanalysis (ERA-40), and Japanese 25-year reanalysis (JRA-25). White zones indicate the missing values masked by topography.

Figure 6 Difference between the temporal correlation coefficients of the seasonal precipitation in the historical experiment and Hadley Centre Global Environmental Model version 2–Atmosphere–Ocean (HadGEM2-AO) over land in March–April–May (MAM), June–July–August (JJA), September–October–November (SON), and December–January–February (DJF) relative to the verification of precipitation. Positive values indicate that the correlation coefficients of the historical experiment are larger than those of HadGEM2-AO.

Figure 7 Differences between the temporal root–mean–square error (RMSE) of seasonal precipitation in the historical experiment and Hadley Centre Global Environmental Model version 2–Atmosphere–Ocean (HadGEM2-AO) over land in March–April–May (MAM), June–July–August (JJA), September–October–November (SON), and December–January–February (DJF) relative to the verification of precipitation. Positive values indicate that the RMSEs of the historical experiment are less than those of HadGEM2-AO.

Figure 8 Near- and far-future significant changes in geopotential height (shading in units of m) and horizontal winds (vector in units of 5 m s^{-1}) at 850 hPa for the Hadley Centre Global Environmental Model version 2–Atmosphere–Ocean (HadGEM2-AO) and Weather Research and Forecasting (WRF) simulations in RCP4.5 and RCP8.5 in March–April–May (MAM). The changes are defined by the departure of each future simulation relative to its simulation of the current climate. White zones indicate missing values masked by the topography. All significant areas are at the 95% confidence level by Student's t-test.

Figure 9 Same as Fig. 8, but for June–July–August (JJA).

Figure 10 Same as Fig. 8, but for September–October–November (SON).

Figure 11 Same as Fig. 8, but for December–January–February (DJF).

Figure 12 Near- and far-future significant changes of precipitation in mm/d of the Hadley Centre Global Environmental Model version 2–Atmosphere–Ocean (HadGEM2-AO) and Weather Research and Forecasting (WRF) simulations in RCP4.5 and RCP8.5 in March–April–May (MAM). The changes are defined by the departure of each future simulation relative to its simulation of the current climate. White zones indicate areas of insignificant changes. All significant areas are at the 95% confidence level by Student's t-test.

Figure 13 Same as Fig. 12, but for June–July–August (JJA).

Figure 14 Same as Fig. 12, but for September–October–November (SON).

Figure 15 Same as Fig. 12, but for December–January–February (DJF).

Figure 16 Near- and far-future precipitation changes of the Hadley Centre Global Environmental Model version 2–Atmosphere–Ocean (HadGEM2-AO) and Weather Research and Forecasting (WRF) projections in RCP4.5 and RCP8.5 in March–April–May (MAM), June–July–August (JJA), September–October–November (SON), and December–January–February (DJF) averaged over the Indo–China Peninsula (IC), Sumatra, Java, Borneo, and New Guinea. The changes are defined by the departure of each future simulation relative to its simulation of the current climate.

Figure 17 Near- and far-future changes of precipitation spatial variability projected by the Hadley Centre Global Environmental Model version 2–Atmosphere–Ocean (HadGEM2-AO) and Weather Research and Forecasting (WRF) models in RCP4.5 and RCP8.5 in March–April–May (MAM), June–July–August (JJA), September–October–November (SON), and December–January–February (DJF) over the Indo–China Peninsula (IC), Sumatra, Java, Borneo, and New Guinea. The changes are defined by the departure of each future simulation relative to its simulation of the current climate.

FIGURES

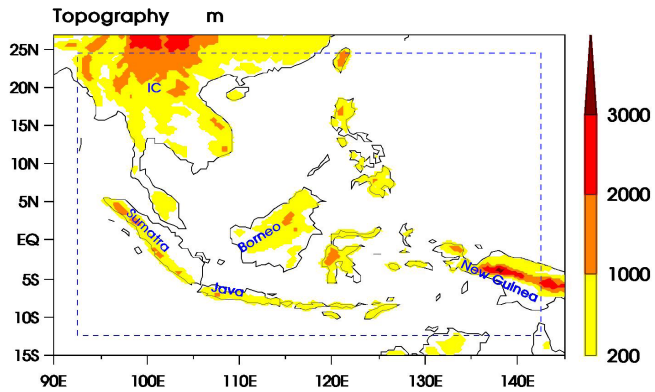

Figure 1. Simulation domain (15°S–27°N, 90–145°E), buffer zone (outside of blue dashed lines:12.5°S–24.5°N, 87.5–142.5°E), and topography (color shading in units of meters). Analysis areas over land enclosed by blue lines refer to IC, Sumatra, Java, Borneo, and New Guinea.

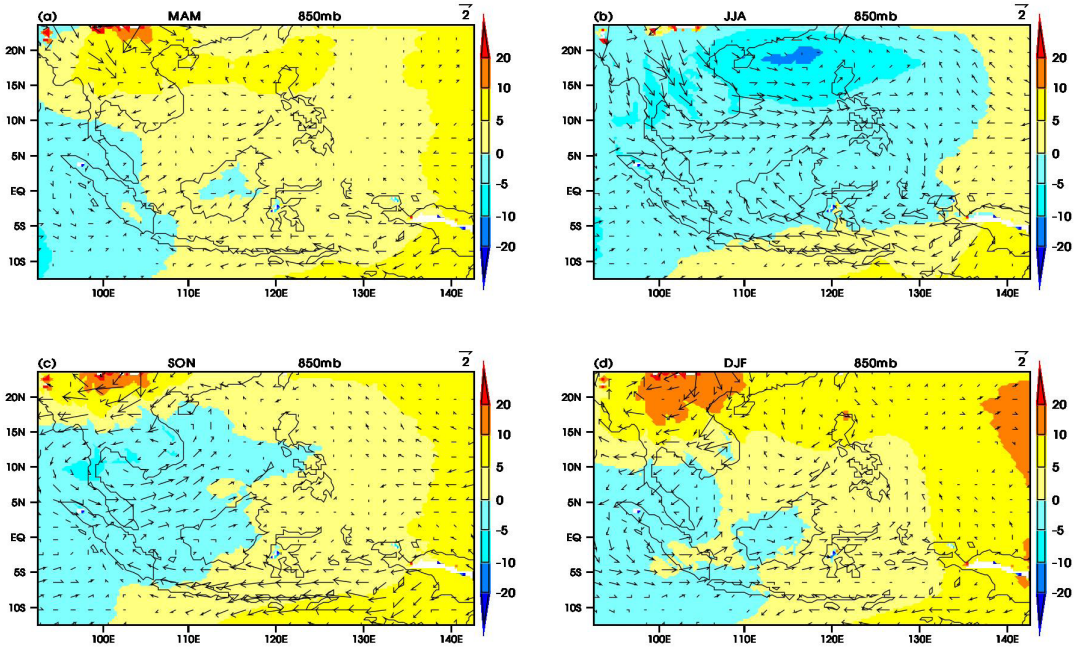

Figure 2. The model biases of geopotential height (shading in units of meter) and horizontal winds (vector in units of 5 m s^{-1}) at 850 hPa in MAM mean (a), JJA mean (b), SON mean (c), and DJF mean (d), in the hindcast experiment forced by ECMWF Interim reanalysis (ERA-Interim). All the biases are defined by the departure of RCM simulations from the large-scale forcing of ensemble mean of the NCEP/DOE reanalysis 2 (NCEP-R2), ERA-40, and the Japanese 25-year reanalysis (JRA-25). White zones are the missing value masked by the topography.

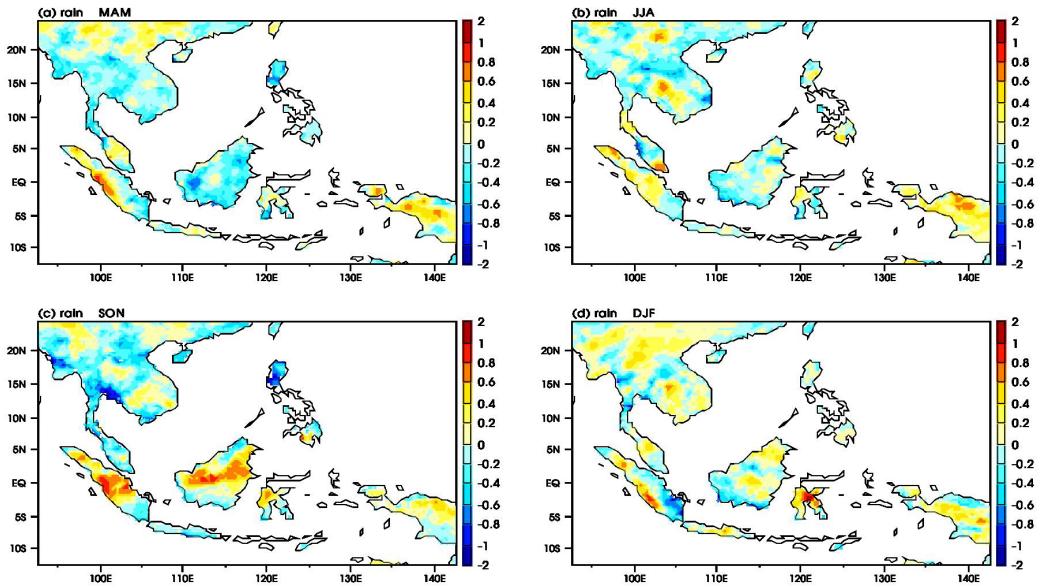

Figure 3. The difference between temporal correlation coefficients of the seasonal precipitation in hindcast experiment and ERA-Interim over land in MAM, JJA, SON, and DJF, relative to the verification precipitation. Positive value means the correlation coefficients of the hindcast experiment is larger than that of the ERA-Interim.

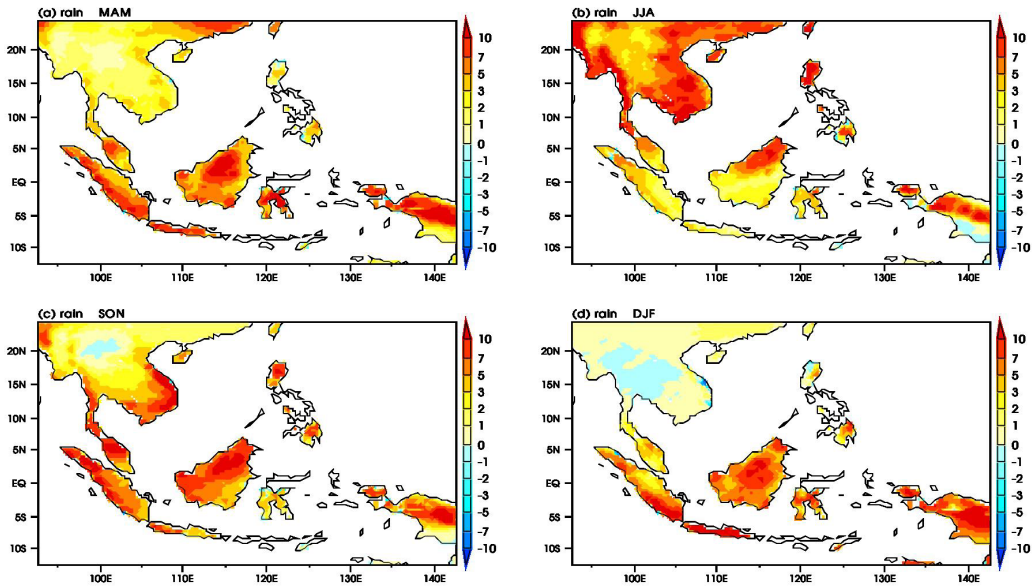

Figure 4. The difference between temporal RMSE of the seasonal precipitation in hindcast experiment and ERA-Interim over land in MAM, JJA, SON, and DJF, relative to the verification precipitation. Positive value means the RMSE of the hindcast experiment is less than that of the ERA-Interim.

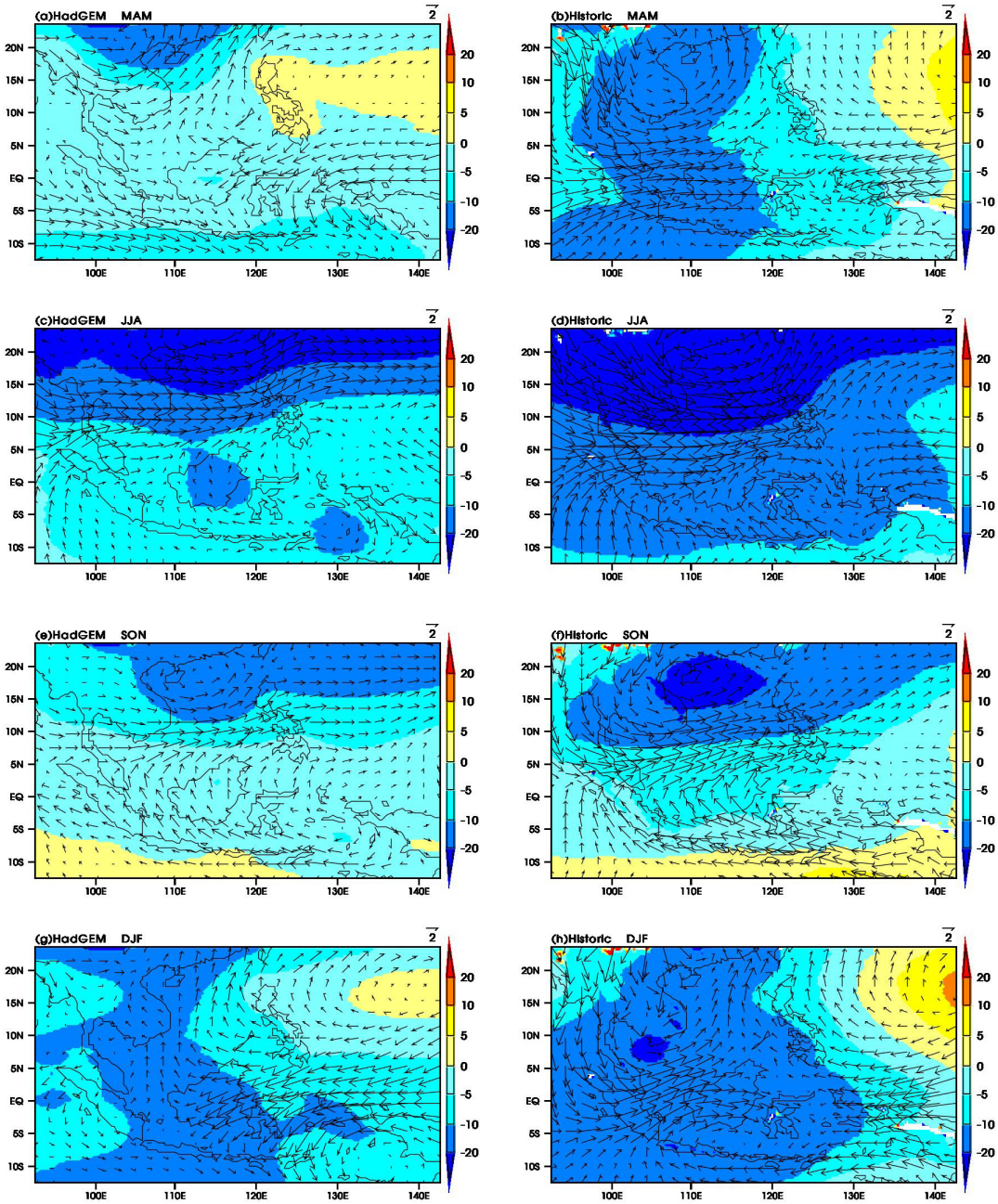

Figure 5. The model biases of geopotential height (shading in units of meter) and horizontal winds (vector in units of 5 m s^{-1}) at 850 hPa of the HadGEM2-AO and historical experiment in MAM mean (a, b), JJA mean (c, d), SON mean (e, f), and DJF mean (g, h). All the biases are defined by the departure from the large-scale forcing of ensemble mean of the NCEP/DOE reanalysis 2 (NCEP-R2), ERA-40, and the Japanese 25-year reanalysis (JRA-25). White zones are the missing value masked by the topography.

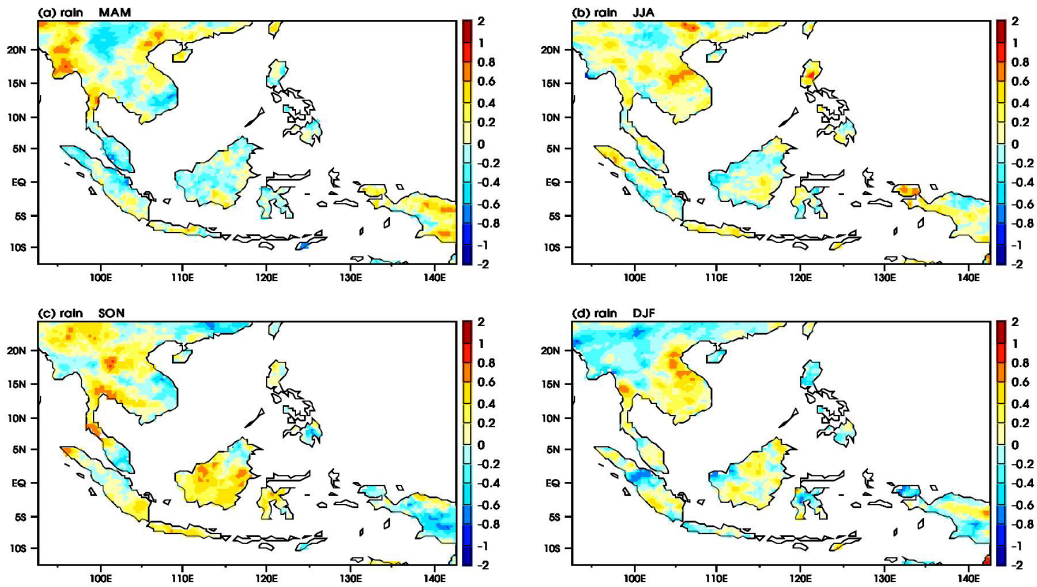

Figure 6. The difference between temporal correlation coefficients of the seasonal precipitation in historical experiment and HadGEM2-AO over land in MAM, JJA, SON, and DJF, relative to the verification precipitation. Positive value means the correlation coefficients of the historical experiment is larger than that of the HadGEM2-AO.

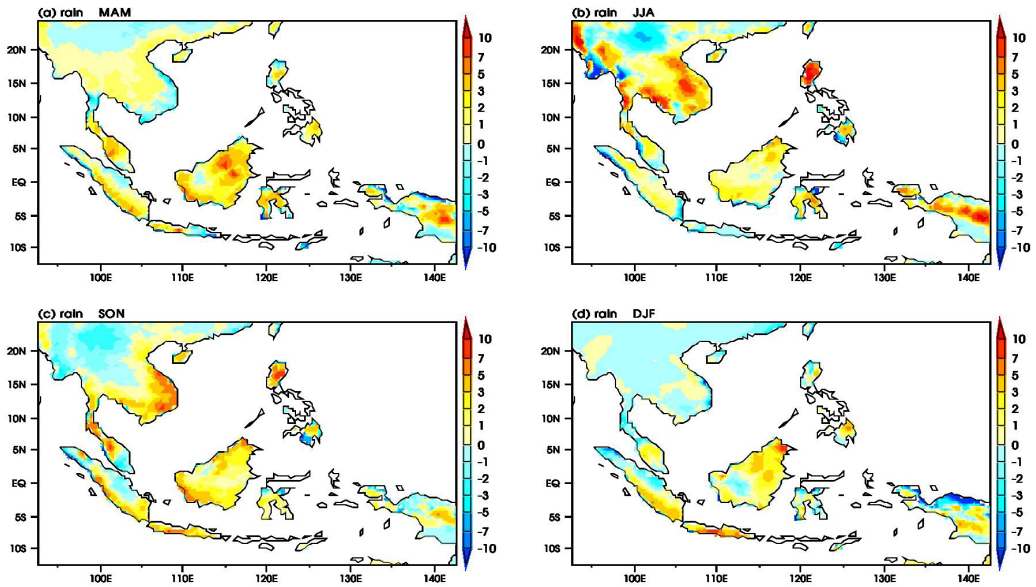

Figure 7. The difference between temporal RMSE of the seasonal precipitation in historical experiment and HadGEM2-AO over land in MAM, JJA, SON, and DJF, relative to the verification precipitation. Positive value means the RMSE of the historical experiment is less than that of the HadGEM2-AO.

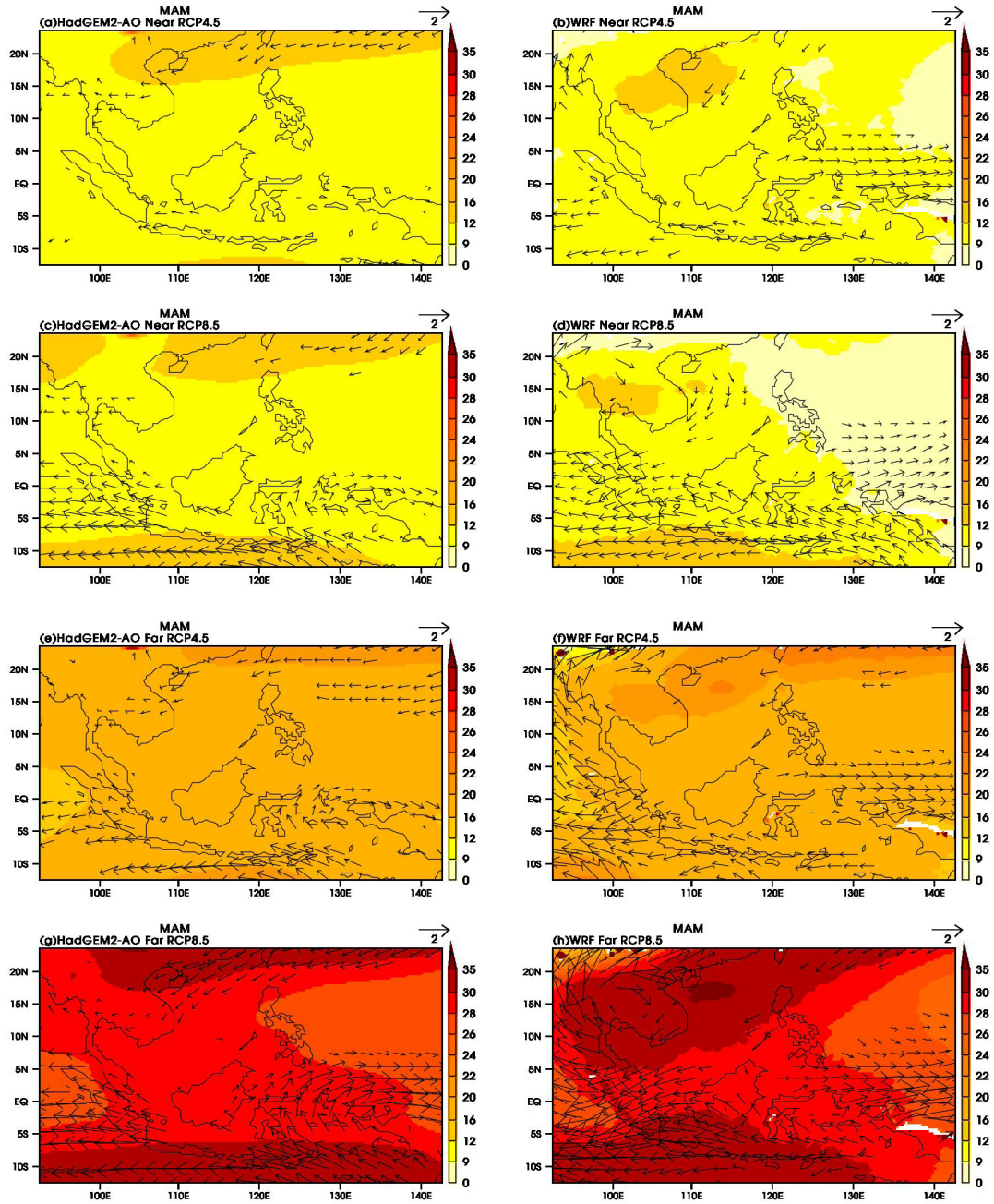

Figure 8. The near and far future significant changes of geopotential height (shading in units of meter) and horizontal winds (vector in units of 5 m s^{-1}) at 850 hPa of the HadGEM2-AO and WRF simulations in RCP4.5 and RCP8.5 in MAM. The changes are defined by the departure of each future simulation relative to its simulation of current climate. White zones are the missing value masked by the topography. All significance areas are at the 95% confidence level by the t-test.

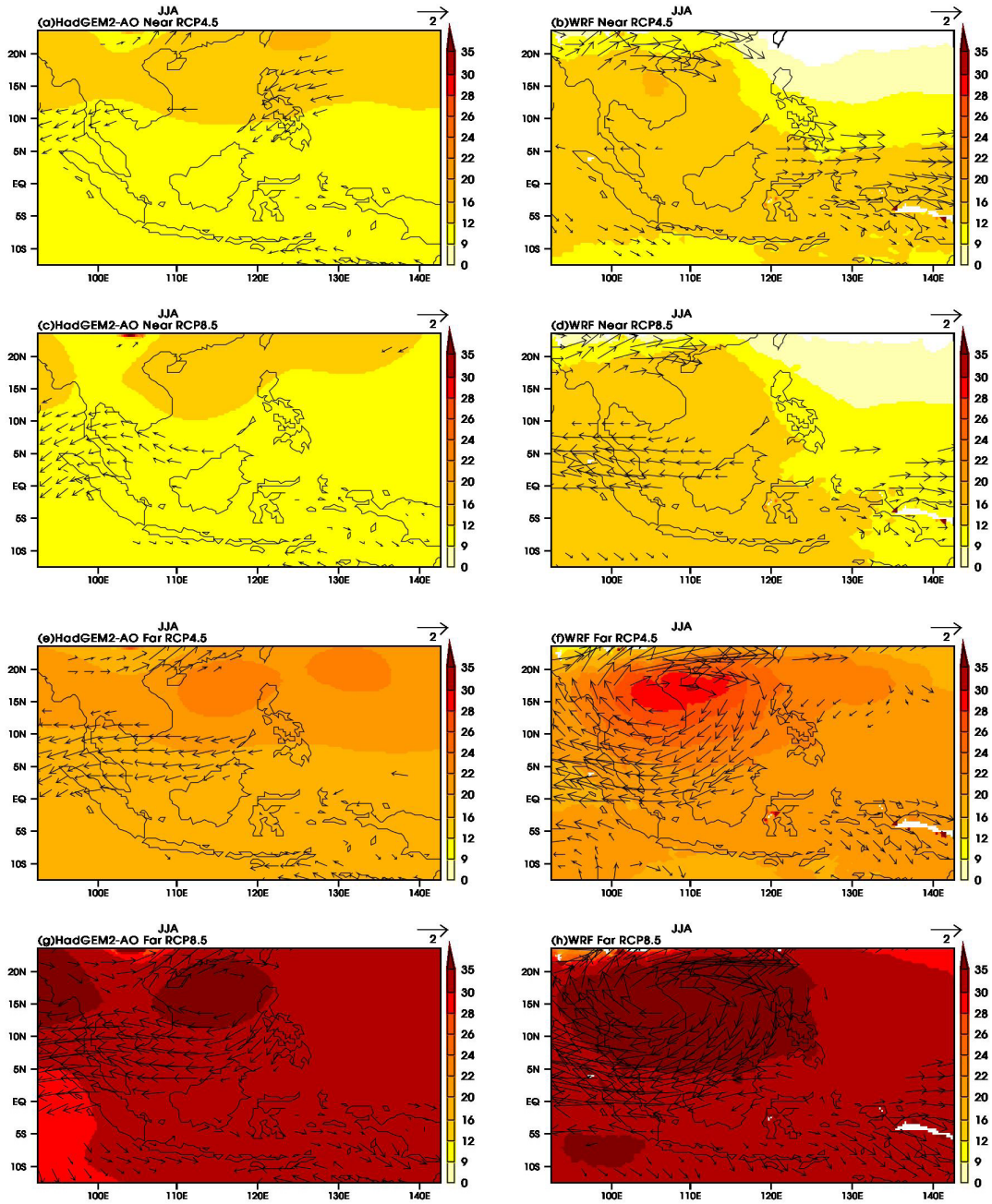

Figure 9. As in Fig. 8, but for JJA.

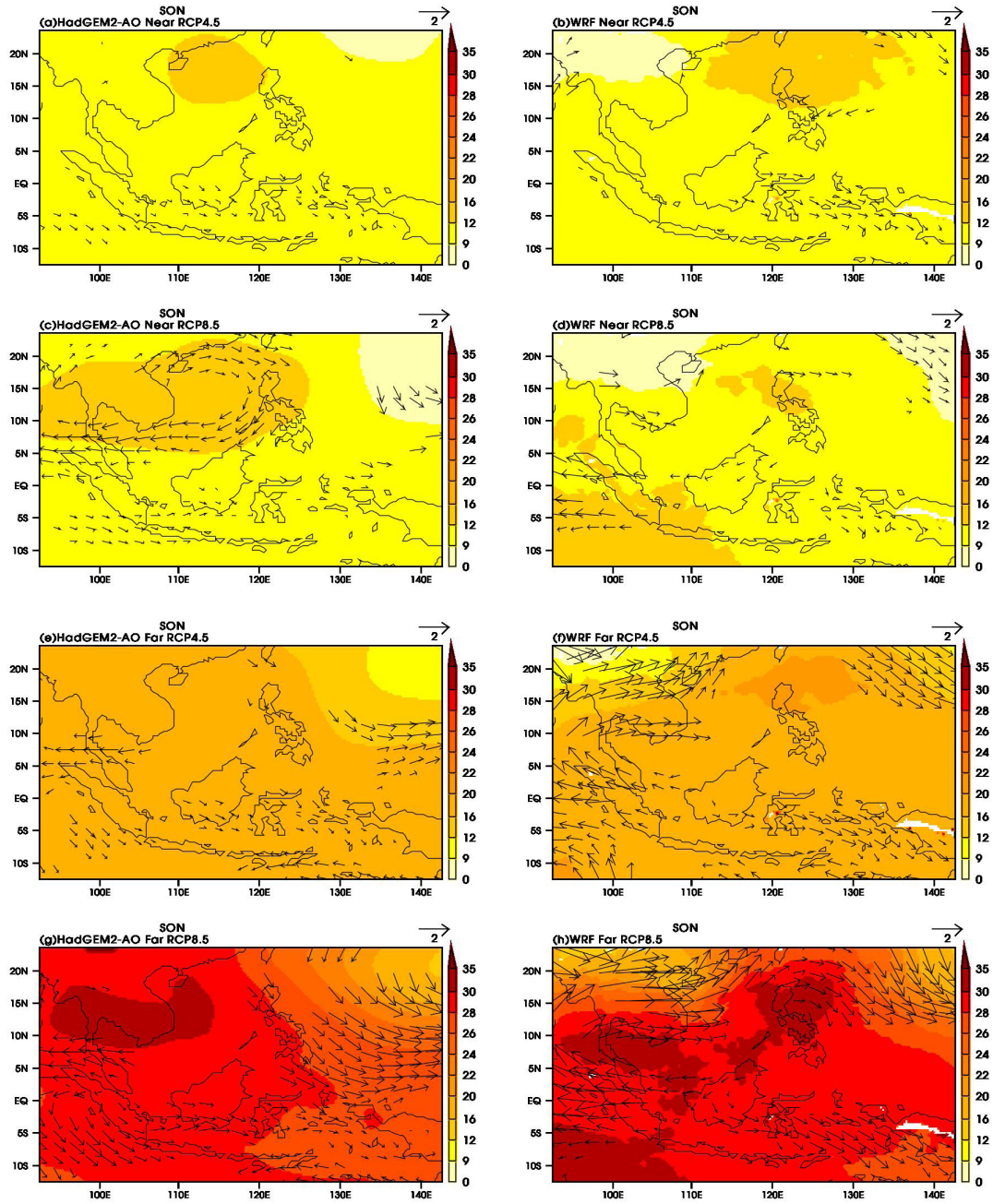

Figure 10. As in Fig. 8, but for SON.

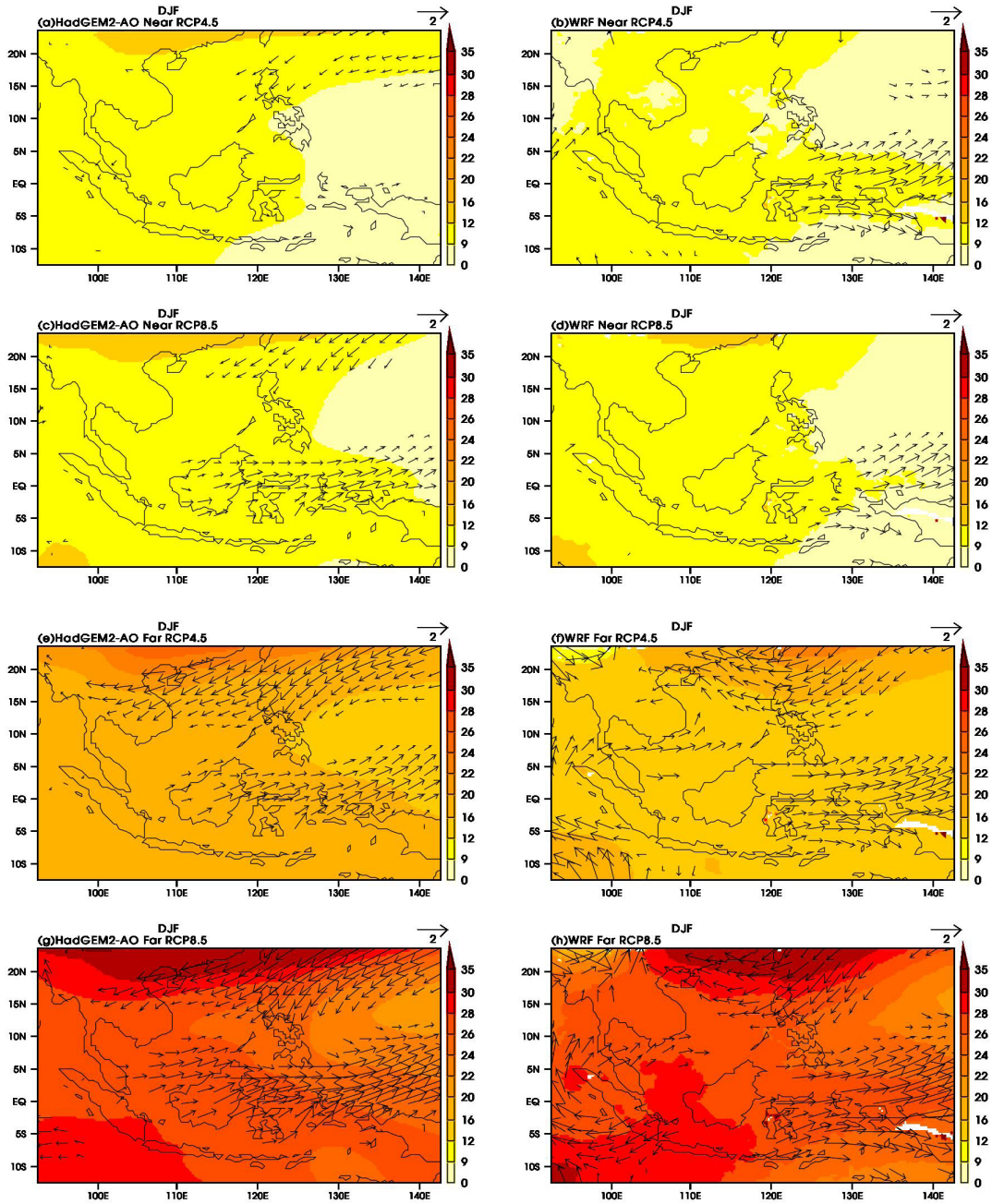

Figure 11. As in Fig. 8, but for DJF.

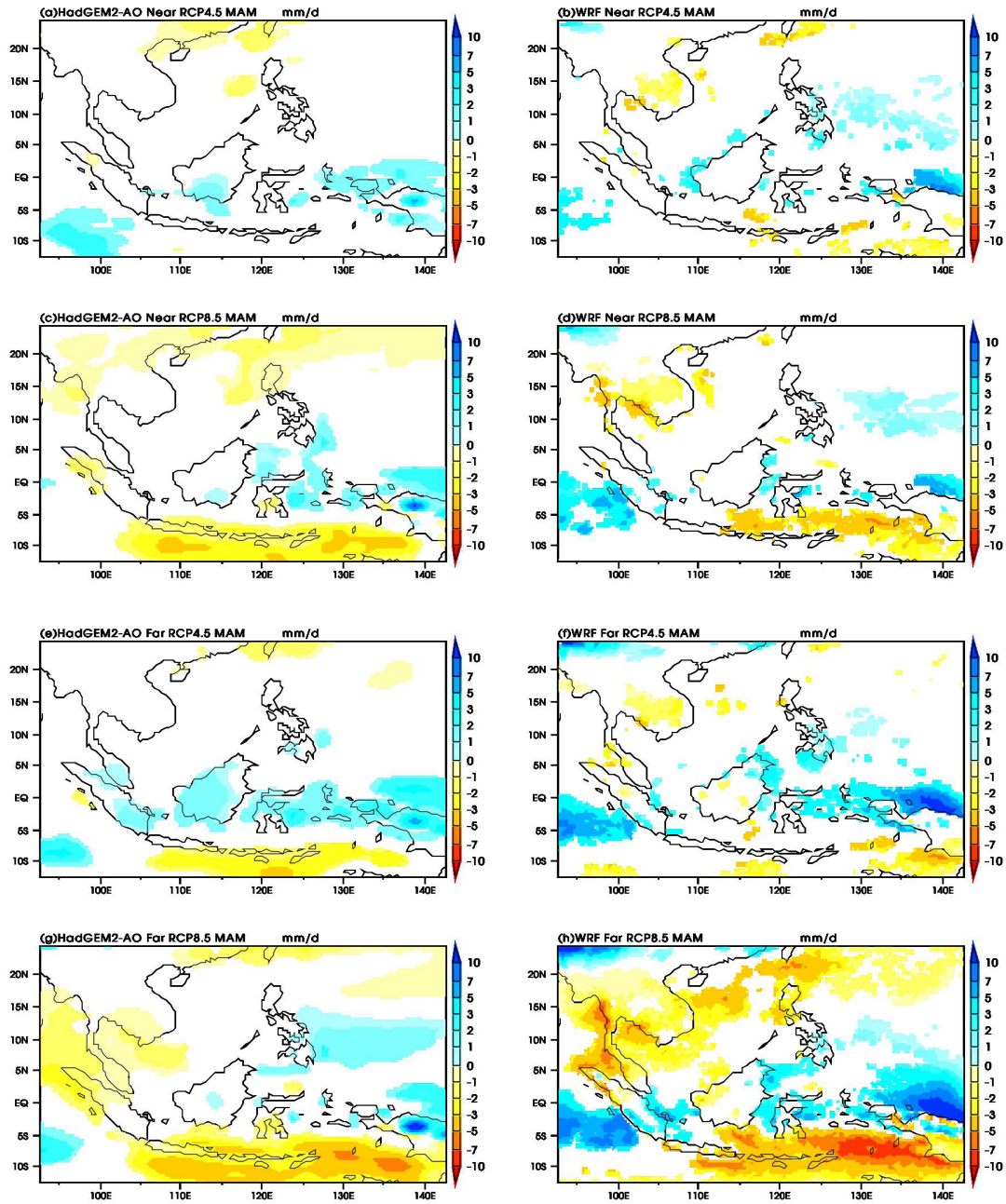

Figure 12. The near and far future significant changes of precipitation in mm/d of the HadGEM2-AO and WRF simulations in RCP4.5 and RCP8.5 in MAM. The changes are defined by the departure of each future simulation relative to its simulation of current climate. White zones are the areas where the change is insignificant. All significance areas are at the 95% confidence level by the t-test.

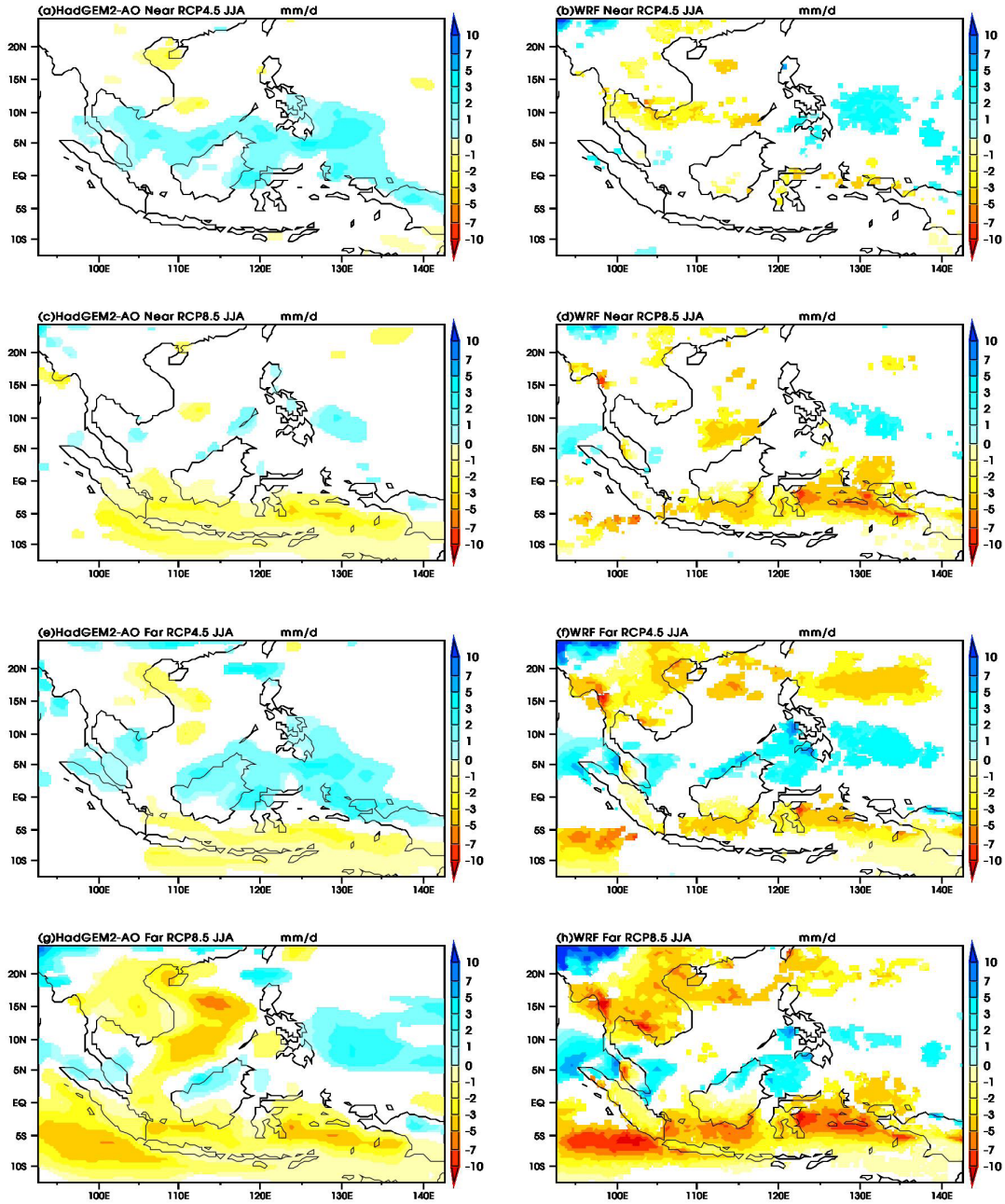

Figure 13. As same as Fig. 12, but for JJA.

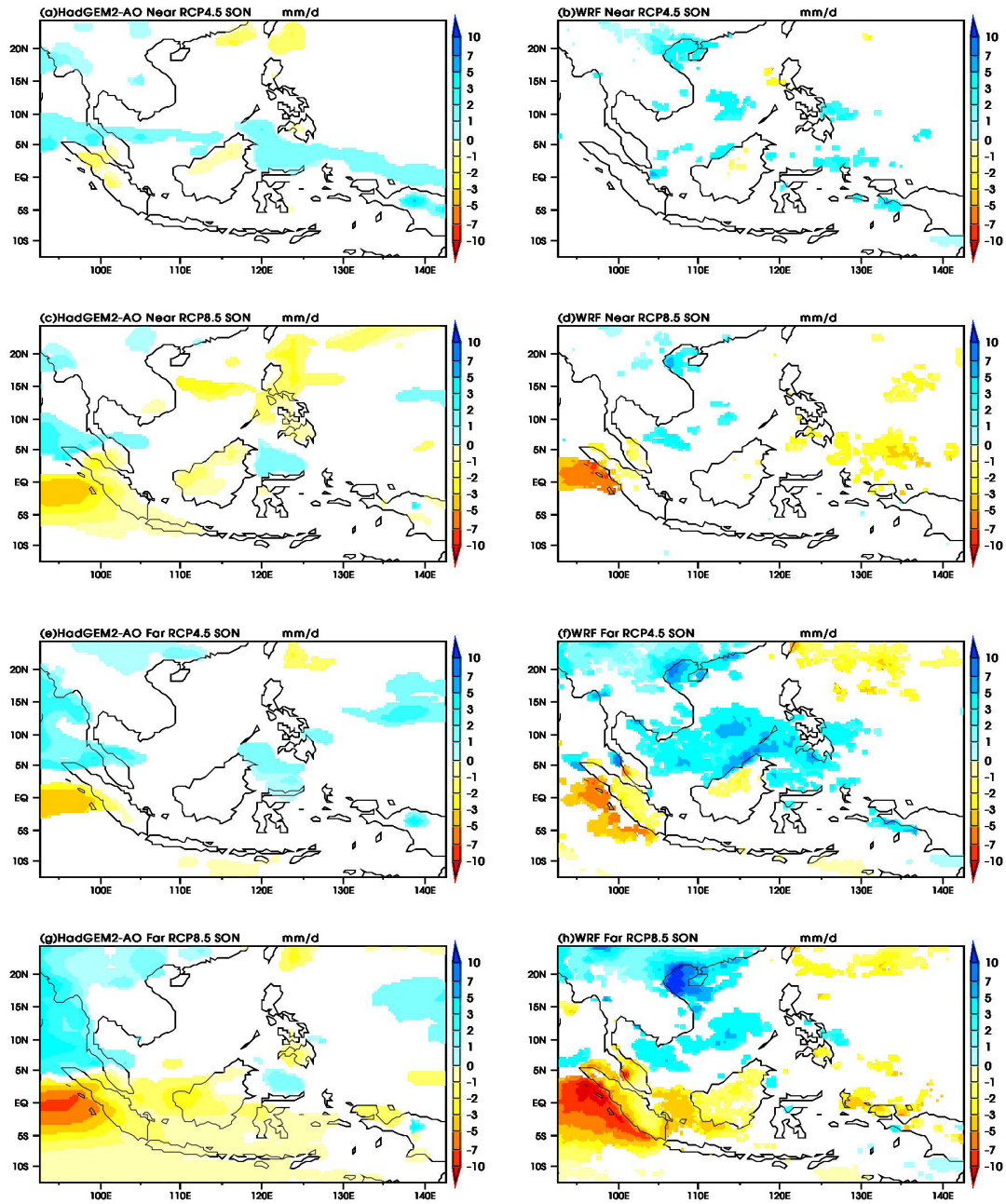

Figure 14. As same as Fig. 12, but for SON.

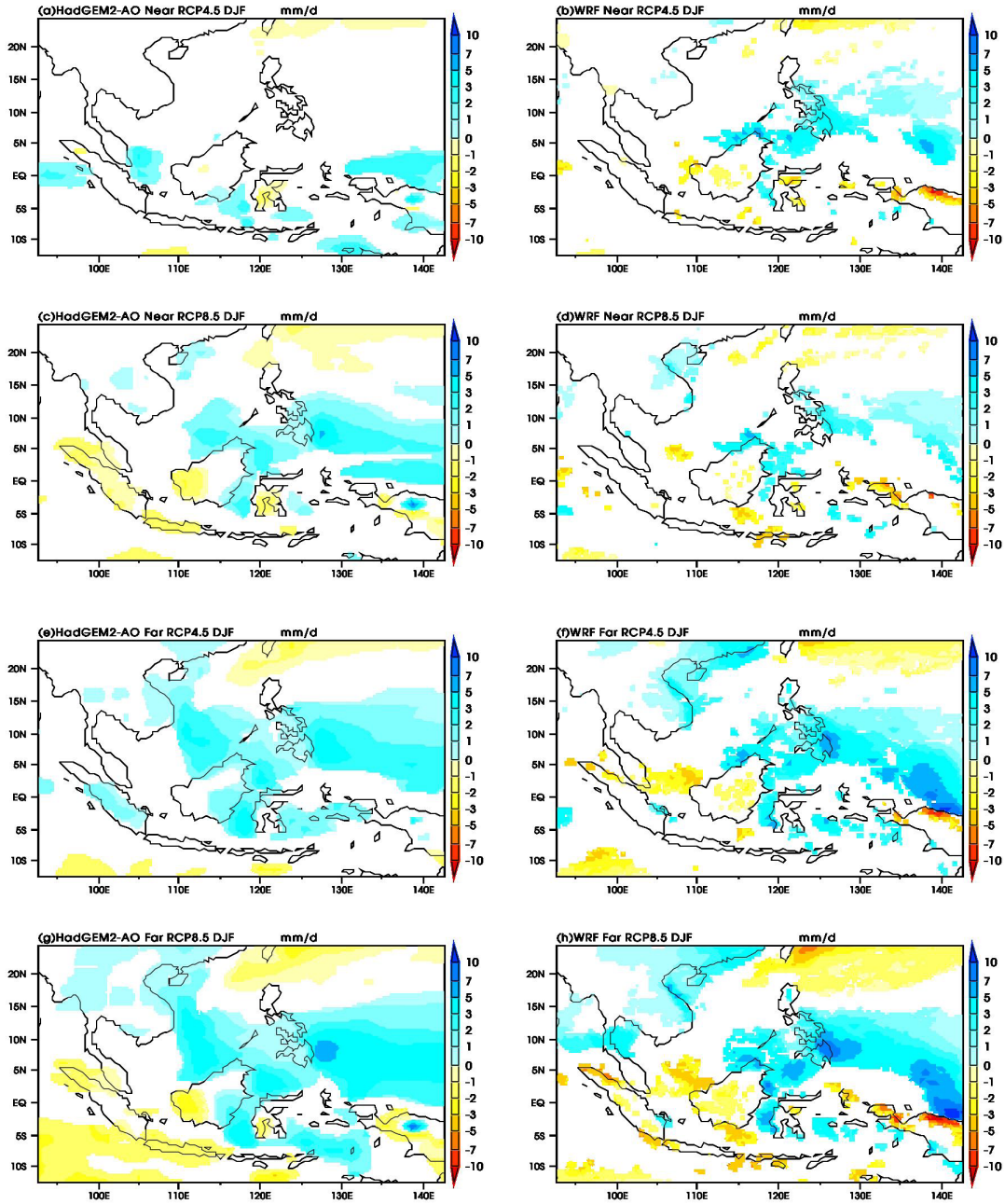

Figure 15. As same as Fig. 12, but for DJF.

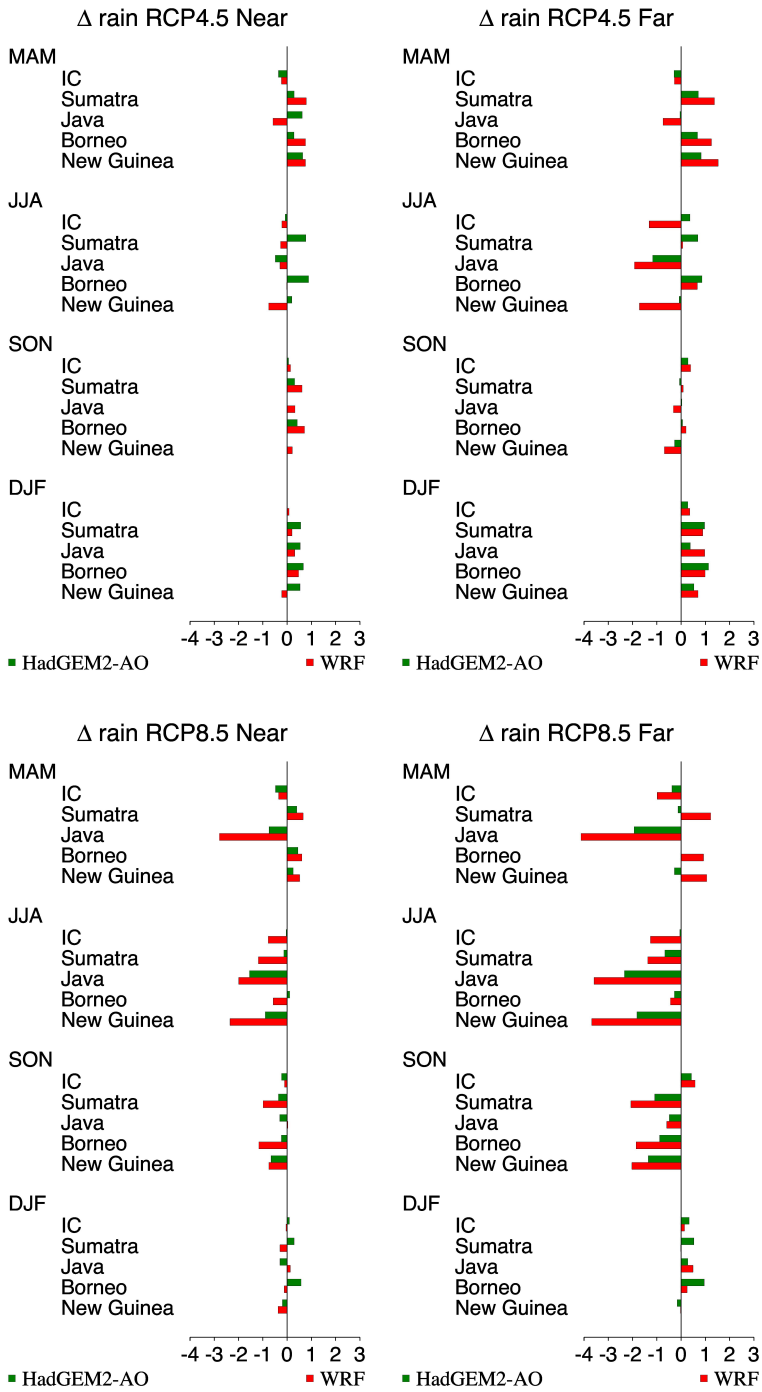

Figure 16. The near and far future precipitation changes of the HadGEM2-AO and WRF projections in RCP4.5 and RCP8.5 in MAM, JJA, SON, and DJF averaged over the IC, Sumatra, Java, Borneo, and New Guinea. The changes are defined by the departure of each future simulation relative to its simulation of current climate.

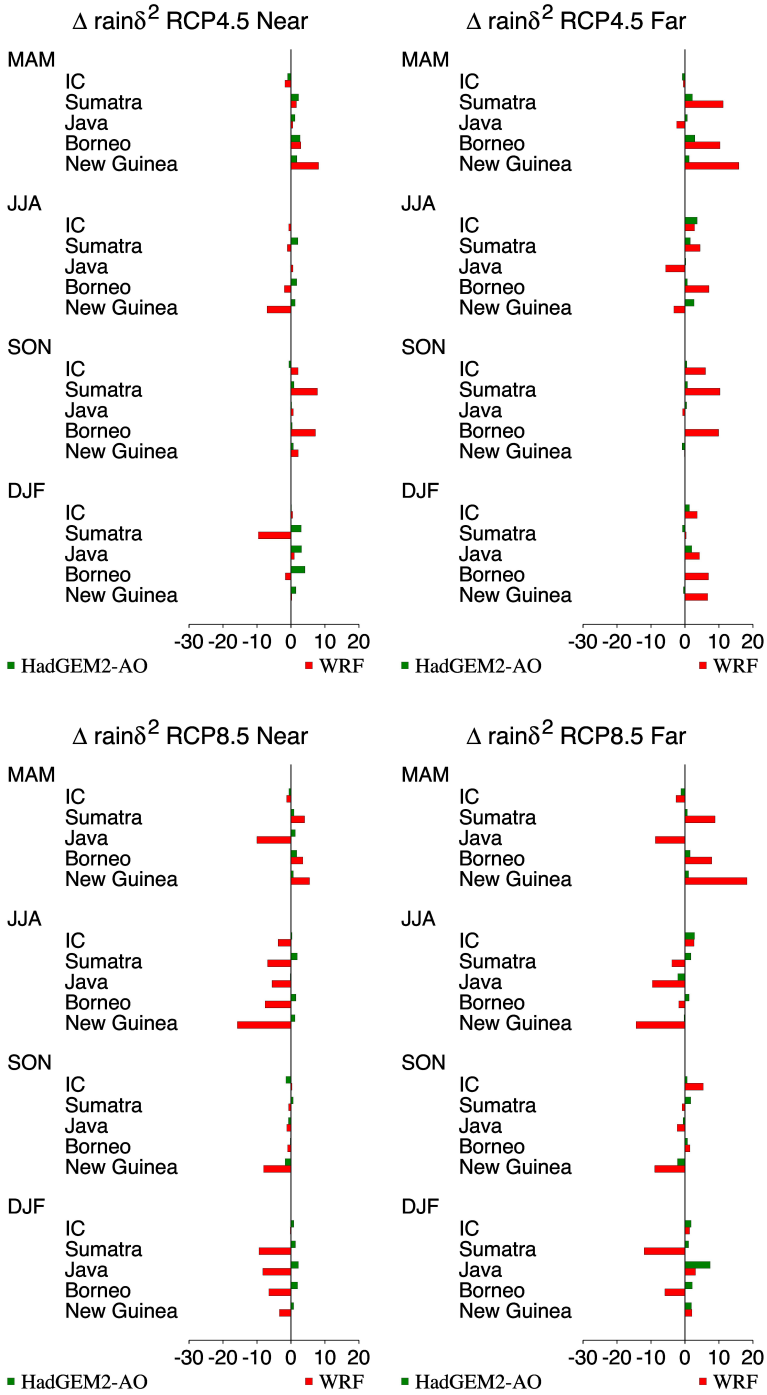

Figure 17. The near and far future changes of precipitation spatial variability projected by the HadGEM2-AO and WRF models in RCP4.5 and RCP8.5 in MAM, JJA, SON, and DJF over the IC, Sumatra, Java, Borneo, and New Guinea. The changes are defined by the departure of each future simulation relative to its simulation of current climate.

RESEARCH REPORT 2015-07

Dynamic Downscaling of Climate Change Over The Maritime Continent

Hongwei Yang Climate Analysis Team

APCC
APEC CLIMATE CENTER

APEC Climate Center
12 Centum 7-ro, Haeundae-gu, Busan 612-020, Republic of Korea
Tel: +82-51-745-3900 Fax: +82-51-745-3949

www.apcc21.org

www.facebook.com/apcc21
www.twitter.com/apcc21
www.flickr.com/apcc21
www.youtube.com/APECClimateCenter21
www.plus.google.com/+APECClimateCenter21